

2 From Materials to Models: Deriving Insight from Bands

Ole Krogh Andersen

Max-Planck-Institut für Festkörperforschung

Stuttgart

Contents

1	Introduction	2
2	Periodic system of the elements	2
3	Band structures of the elemental metals	7
3.1	Separating structure and potential	7
3.2	Force theorem, pressures, and structures	16
3.3	Band magnetism	20
3.4	Fermi surfaces and mass renormalizations	28
4	Post 1986	29
4.1	ARPES	30
4.2	Static and dynamical mean-field approximations	31
4.3	Transition-metal oxides (TMOs)	32
4.4	Elemental metals	35

1 Introduction

In contrast to most other lectures in this Autumn-School series on Correlated Electrons, this one will deal little with recent theories of how to describe and compute observables for correlated materials, but mostly with insights derived a while ago from bands, not even quasiparticle excitations, but merely Hohenberg-Kohn-Sham eigenvalues, Kohn's "bastards of DFT". After scanning through previous year's lectures and recent papers, I felt that this might not be entirely inappropriate.

2 Periodic system of the elements

The most fundamental chemical insight ever derived from one-electron energies is Bohr's theory of the periodic system of the elements [1]. I therefore found it appropriate to start with a reminder about the electronic structure of atoms (see also Refs. [2–5]).

Materials are made of atoms, and atoms are (almost) round. The electronic structure of an atom can therefore be constructed from atomic orbitals, $\varphi_l(\varepsilon_{nl}, r) Y_{lm}(\hat{\mathbf{r}}) \chi_\sigma(s)$, which are the solutions of the one-electron Schrödinger equation in the spherically symmetric, self-consistent potential, $v(r)$, from the attractive protons in the nucleus and the repulsive (other) electrons in the atomic shells. $\chi_\sigma(s)$ are the spin functions which are the eigenfunctions of \hat{s}_z , $Y_{lm}(\hat{\mathbf{r}})$ are the spherical harmonics which are eigenfunctions of \hat{l}^2 and \hat{l}_z , and the radial functions satisfy the radial Schrödinger equations,

$$- (r\varphi_l(\varepsilon_{nl}, r))'' = (\varepsilon_{nl} - v_l(r)) r\varphi_l(\varepsilon_{nl}, r), \text{ with } v_l(r) \equiv v(r) + l(l+1)/r^2 \quad (1)$$

(in atomic Rydberg units) with the boundary conditions that $\varphi(r)$ be regular at the origin and vanish at infinity. The potentials $v(r) = v_s(r)$ and $v_d(r)$ are shown in Fig. 3 for a neutral Pt atom in weak lines.

For given l , the solutions of (1) are numbered in order of increasing energy, ε_{nl} , by the principal quantum number, n , which takes the values $l+1, l+2, \dots$, because with this convention, the energy levels for a Coulomb potential, $-2Z/r$, are independent of l and given by $\varepsilon_{nl} = -(Z/n)^2$, Bohr's formula from 1913, before quantum mechanics. The radial functions decay at large distances as $\exp(-Zr/n)$ and the number of nodes in the radial function is $n-l-1$.

For a neutral atom with Z protons in the nucleus and Z electrons in the shells, the effective charge defined in terms of the self-consistent potential through: $Z_{\text{eff}}(r) \equiv -rv(r)/2$, decreases from the value Z , towards 1 as r increases from 0 to ∞ due to the screening by the (other) electrons. As a consequence, the $2(2l+1)$ -degeneracy of the attractive Coulomb potential is lifted and the perturbation by the repulsive centrifugal potential, $l(l+1)/r^2$, will cause the one-electron energies for the same n to increase with l : $\varepsilon_{ns} < \varepsilon_{np} < \varepsilon_{nd} < \dots$. Whereas the order of the s - and p -energies is always such that $\varepsilon_{ns} < \varepsilon_{np} < \varepsilon_{(n+1)s}$, the order of the d -energies is such that $\varepsilon_{(n+1)s} < \varepsilon_{nd}$ when the nd -shell is empty, and such that $\varepsilon_{np} < \varepsilon_{nd} < \varepsilon_{(n+1)s}$ when the nd -shell is full. Analogously, $\varepsilon_{nd} < \varepsilon_{(n-1)f}$ when the $(n-1)$ f -shell is empty, and $\varepsilon_{(n-1)d} < \varepsilon_{(n-1)f} < \varepsilon_{nd}$ when the $(n-1)$ f -shell is full.

Periodic Table, with the Outer Electron Configurations of Neutral Atoms in Their Ground States
 The notation used to describe the electronic configuration of atoms and ions is discussed in all textbooks of introductory atomic physics. The letters *s*, *p*, *d*, . . . signify electrons having orbital angular momentum 0, 1, 2, . . . in units \hbar ; the number to the left of the letter denotes the principal quantum number of one orbit, and the superscript to the right denotes the number of electrons in the orbit.

Li³	Be⁴											B⁵	C⁶	N⁷	O⁸	F⁹	Ne¹⁰
2s	2s ²											2s ² 2p	2s ² 2p ²	2s ² 2p ³	2s ² 2p ⁴	2s ² 2p ⁵	2s ² 2p ⁶
Na¹¹	Mg¹²											Al¹³	Si¹⁴	P¹⁵	S¹⁶	Cl¹⁷	Ar¹⁸
3s	3s ²											3s ² 3p	3s ² 3p ²	3s ² 3p ³	3s ² 3p ⁴	3s ² 3p ⁵	3s ² 3p ⁶
K¹⁹	Ca²⁰	Sc²¹	Ti²²	V²³	Cr²⁴	Mn²⁵	Fe²⁶	Co²⁷	Ni²⁸	Cu²⁹	Zn³⁰	Ga³¹	Ge³²	As³³	Se³⁴	Br³⁵	Kr³⁶
4s	4s ²	3d	3d ²	3d ³	3d ⁵	3d ⁵	3d ⁶	3d ⁷	3d ⁸	3d ¹⁰	3d ¹⁰	4s ² 4p	4s ² 4p ²	4s ² 4p ³	4s ² 4p ⁴	4s ² 4p ⁵	4s ² 4p ⁶
Rb³⁷	Sr³⁸	Y³⁹	Zr⁴⁰	Nb⁴¹	Mo⁴²	Tc⁴³	Ru⁴⁴	Rh⁴⁵	Pd⁴⁶	Ag⁴⁷	Cd⁴⁸	In⁴⁹	Sn⁵⁰	Sb⁵¹	Te⁵²	I⁵³	Xe⁵⁴
5s	5s ²	4d	4d ²	4d ⁴	4d ⁵	4d ⁶	4d ⁷	4d ⁸	4d ¹⁰	4d ¹⁰	4d ¹⁰	5s ² 5p	5s ² 5p ²	5s ² 5p ³	5s ² 5p ⁴	5s ² 5p ⁵	5s ² 5p ⁶
Cs⁵⁵	Ba⁵⁶	La⁵⁷	Hf⁷²	Ta⁷³	W⁷⁴	Re⁷⁵	Os⁷⁶	Ir⁷⁷	Pt⁷⁸	Au⁷⁹	Hg⁸⁰	Tl⁸¹	Pb⁸²	Bi⁸³	Po⁸⁴	At⁸⁵	Rn⁸⁶
6s	6s ²	5d	4f ¹⁴ 5d ²	5d ³	5d ⁴	5d ⁵	5d ⁶	5d ⁹	5d ⁹	5d ¹⁰	5d ¹⁰	6s ² 6p	6s ² 6p ²	6s ² 6p ³	6s ² 6p ⁴	6s ² 6p ⁵	6s ² 6p ⁶
Fr⁸⁷	Ra⁸⁸	Ac⁸⁹															
7s	7s ²	6d	7s ²	Ce⁵⁸	Pr⁵⁹	Nd⁶⁰	Pm⁶¹	Sm⁶²	Eu⁶³	Gd⁶⁴	Tb⁶⁵	Dy⁶⁶	Ho⁶⁷	Er⁶⁸	Tm⁶⁹	Yb⁷⁰	Lu⁷¹
				4f ²	4f ³	4f ⁴	4f ⁵	4f ⁶	4f ⁷	4f ⁷	4f ⁸	4f ¹⁰	4f ¹¹	4f ¹²	4f ¹³	4f ¹⁴	4f ¹⁴
				6s ²	6s ²	6s ²	6s ²	6s ²									
				Th⁹⁰	Pa⁹¹	U⁹²	Np⁹³	Pu⁹⁴	Am⁹⁵	Cm⁹⁶	Bk⁹⁷	Cf⁹⁸	Es⁹⁹	Fm¹⁰⁰	Md¹⁰¹		Lw¹⁰³
				5f ²	5f ²	5f ³	5f ⁴	5f ⁶	5f ⁷	5f ⁷	5f ⁷						
				6d ²	6d												
				7s ²													

Fig. 1: Periodic Table of the Elements. From Ref. [6].

If we now occupy the orbitals, of which there are $2(2l+1)$ per nl -subshell, with Z electrons in order of increasing energy, we recover the Periodic Table, which has one entry for each value of Z increasing in steps of 1 along one row after the other (Fig. 1). The rows are numbered by the period, n , which is the principal quantum number of the outermost s -electron. As Z increases, the first term of the radial potential, $-2Z_{\text{eff}}(r)/r+l(l+1)/r^2$, in Eq. (1) deepens and counteracts the repulsive second term such that bound states occur if $Z \geq 5$ (B), 21 (Sc), and 58 (Ce), for $l=1, 2$, and 3, respectively. This leads to the insertion of the p -, d -, and f -series, whereby the length of the period (number of one-electron states in the n -shell) becomes $2(l_{\text{max}}+1)^2$.

In the columns are the elements with similar chemical properties, and Fig. 1 gives the configuration, i.e., the numbers of electrons in the outer shells for the ground states of the neutral atoms. With increasing l , the radial potential-well becomes more narrow and with it, the region where $\varepsilon_{nl} > v_l(r)$, i.e., which is classically-allowed (see Fig. 3). This increased localization of the orbitals with higher l leads to their decreased chemical activity and, hence, the very similar chemical properties of the rare earths and of the actinides which are exclusively associated with their outer s -, p -, and possibly d -electrons.

When, in the process of filling the nl -subshell, we move from one element to the next, the added nl -electron will partly screen out the added proton. Specifically, the increase of $Z_{\text{eff}}(r)$ is 1 for r in the region near the nucleus which is classically forbidden [$v_l(r) > \varepsilon_{nl}$] for an nl -electron,

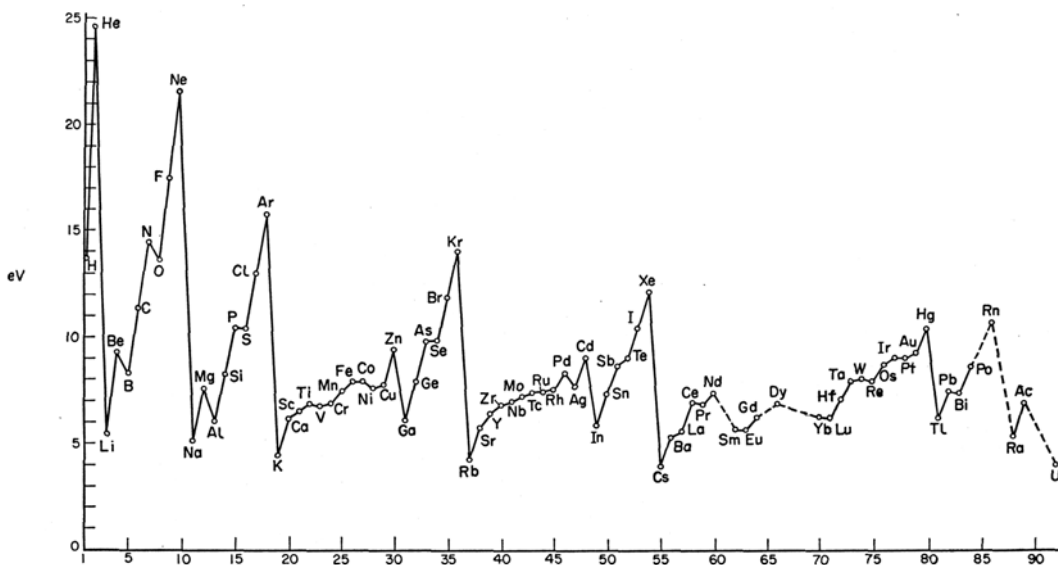


Fig. 2: First ionization potentials as a function of Z . From Ref. [2].

trails off in the classically-allowed region, and vanishes outside. Hence, ε_{nl} will fall a bit, and $\varphi_l(\varepsilon_{nl})$ will contract.

When the filling of the nl -subshell is completed and we start to fill into the next, $n'l'$ -subshell, the increase of $Z_{\text{eff}}(r)$ by unity does not start to trail off before r reaches the region allowed for an $n'l'$ -electron. If $n' \geq n$, this is outside the region of an nl -electron and ε_{nl} will therefore drop sharply and $\varphi_l(\varepsilon_{nl})$ contract rapidly, the nl -shell thereby starts to become part of the core. The Fermi level, ε_F , will jump up, from ε_{nl} to $\varepsilon_{n'l'}$. This is what happens most dramatically when going from $ns^2 np^6$ to $ns^2 np^6 (n+1)s^1$, i.e., from an inert gas to an alkali metal, and far less dramatically when going from ns^2 to $ns^2 np^1$, i.e., from Be to B, from Mg to Al, from Zn to Ga, from Cd to In, and from Hg to Tl. In the last three cases the upwards jumps are larger because, here, also the full $(n-1)d^{10}$ shell contracts. This shell structure is clearly seen in Fig. 2 showing for increasing Z the experimental first ionization potential. In theory, this is the ground-state energy of the positive ion minus that of the neutral atom. Neglecting multiplet effects and using the transition-state potential [7], it is simply $-\varepsilon_F$.

For an nd -shell, ε_{nd} continues to drop after the nd band is full, i.e., when going from $nd^{10}(n+1)s^1$ to $nd^{10}(n+1)s^2$, i.e., from Cu to Zn, from Ag to Cd, and from Au to Hg. This is because the $(n+1)s$ shell contracts as it gets filled and drags the nd shell along.

The abrupt behaviors observed when we start to fill into the $n'l'$ -subshell do not occur if $n' < n$, because now $\varphi_{l'}(\varepsilon_{n'l'})$ lies inside $\varphi_l(\varepsilon_{nl})$. This is the case at the beginning of a transition series when going from ns^2 to $ns^2 (n-1)d^1$, i.e., from Ca to Sc, from Sr to Y, from Ba to La, or from Ra to Ac. Filling the more localized $(n-1)d$ -shell, e.g., going from $ns^2 (n-1)d^1$ to $ns^2 (n-1)d^2$, hardly influences the ns energies and orbitals, ε_{ns} and $\varphi_s(\varepsilon_{ns})$. As $\varepsilon_{(n-1)d}$ gradually drops, it will therefore at some stage reach ε_{ns} whereby some of the electrons in the ns -shell may be transferred into the $(n-1)d$ -shell. After the filling of the $(n-1)d$ -shell has been completed, the filling of the ns shell will be resumed. The same holds for ε_{nd} and $\varphi_d(\varepsilon_{nd})$ when filling the $(n-1)f$ -shell in lanthanide or actinide series.

The positions and widths of the sp - and d -bands in the elemental, closely-packed transition metals follow the same trends as the one-electron energies and orbitals described above. Also the relative positions of O p -bands and transition-metal d -bands in transition-metal oxides are roughly in accord with the ionization potentials in Fig. 2. Periodic Tables of the elements containing information about bands in solids may be found in Refs. [8–12] and [4].

The relativistic effects may for the purpose of conceptual simplicity and with little loss of accuracy be included by *formally* using the Pauli Hamiltonian,

$$H = -\nabla^2 + v(r) - \frac{1}{c^2} \left((\varepsilon - v(r))^2 + v'(r) \frac{\partial}{\partial r} - \frac{v'(r)}{r} 2\hat{s} \cdot \hat{\mathbf{I}} \right). \quad (2)$$

Of the relativistic terms ($\propto c^{-2}$) the two first, the mass-velocity and the Darwin term are diagonal in the $lm\sigma$ -representation and may therefore be included in the radial equation for $\varphi_l(\varepsilon, r)$. But the last, the spin-orbit(SO)-coupling term is not diagonal because

$$\langle l'm' | 2\hat{s} \cdot \hat{\mathbf{I}} | lm \rangle = \begin{pmatrix} m \delta_{m'm} & \sqrt{(l+m)(l-m+1)} \delta_{m'(m-1)} \\ \sqrt{(l-m)(l+m+1)} \delta_{m'(m+1)} & -m \delta_{m'm} \end{pmatrix} \delta_{l'l} \quad (3)$$

in the \uparrow, \downarrow -representation. Since the atom is round, $\hat{j} \equiv \hat{\mathbf{I}} + \hat{s}$ is conserved, so that \hat{l}^2 , \hat{s}^2 , \hat{j}_z , and \hat{j}^2 , are good quantum numbers whose eigenvalues are specified by respectively l , $s = \frac{1}{2}$, $\mu = m \pm \frac{1}{2}$, and $j = l \pm \frac{1}{2}$. From:

$$j(j+1) = \hat{j} \cdot \hat{j} = \hat{\mathbf{I}} \cdot \hat{\mathbf{I}} + \hat{s} \cdot \hat{s} + 2\hat{s} \cdot \hat{\mathbf{I}} = l(l+1) + 3/4 + 2\hat{s} \cdot \hat{\mathbf{I}}$$

we then see that

$$2\hat{s} \cdot \hat{\mathbf{I}} = -(1 + \kappa) = \begin{cases} l & \text{when } j = \begin{cases} l + \frac{1}{2} \\ l - \frac{1}{2} \end{cases} \\ -(l+1) & \end{cases}.$$

Changing to the Pauli spinor representation, $\varphi_\kappa(\varepsilon, r) Y_{\kappa\mu}(\hat{\mathbf{r}}\sigma)$, the radial equation for $r \varphi_\kappa(\varepsilon, r)$ is (1), but with

$$\frac{1}{c^2} \left((\varepsilon - v(r))^2 - \frac{v''(r)}{2} - \frac{v'(r)}{r} + (1 + \kappa) \frac{v'(r)}{r} \right) \quad (4)$$

subtracted from the potential, $v(r)$.

The relativistic terms are seen to have their origin in the regions close to the nuclei where the velocity of the electron is high. Hence, they increase with increasing probability that the electron is near the nucleus; that is, with *increasing* Z (approximately $\propto Z^2$) for a given nl -shell, and with *decreasing* n and l for a given Z . The first term in Eq. (4), which is caused by the increase of the electron's mass with velocity, is always lowering its energy. The second term, which may be interpreted as the correction of the electron's potential energy due to its finite extent of the order of the Compton wavelength h/m_0c , raises the energy of s -electrons, but is negligible for higher l . Those two first terms are by far the largest. They can be treated essentially exactly by exchanging the radial Schrödinger equation (1) by the radial *scalar* Dirac equation, which is like the perturbative Pauli equation (4), but without its last, SO-coupling term [13]. That

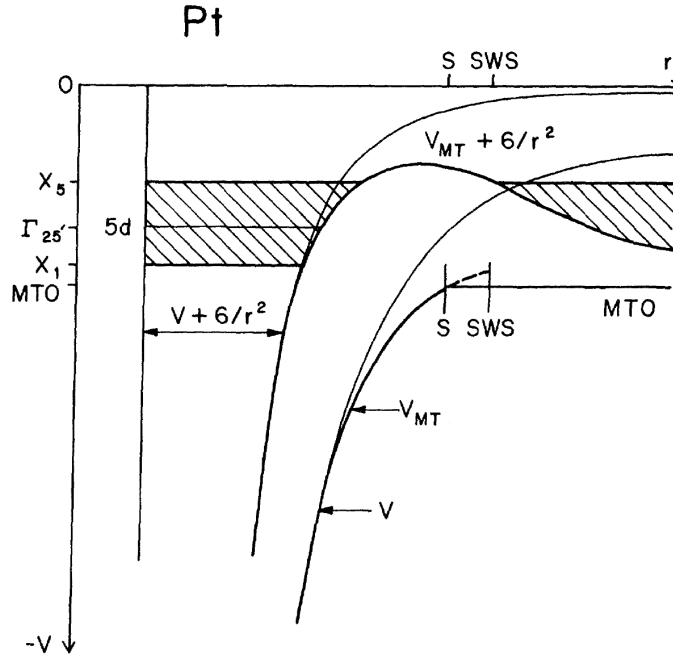


Fig. 3: Energies, ε_{5d} , and potentials, $v(r)$ and $v_d(r)$, entering the radial Schrödinger equation (1) for atomic and fcc Pt in respectively weak and solid lines. The potentials are lined up close to the nucleus. MTO is the MT zero. S and SWS are respectively the MT and the WS radius. The latter is denoted s in the following. $1 \text{ Ry} = 13.6 \text{ eV}$. From Ref. [15].

term, $\xi \hat{s} \cdot \hat{l}$, is then added as in the Pauli Hamiltonian (2), but the parameter, $\xi_l(\varepsilon)$, is obtained accurately from the proper two coupled radial Dirac-equations [14]. The transition-metal band edges and the SO coupling parameters for the nd -bands shown respectively in Figs. 7 and 10 in the next section were calculated using the radial Dirac equations.

Finally, a brief reminder about the many-electron wavefunctions and energies of atoms: The configurations given in the Periodic Table specify the occupations of the open nl -subshells. Due to the $2(2l+1)$ -fold m - and σ -degeneracy of such a shell, several Slater determinants corresponding to the various possible occupancies of m and σ may be formed for this configuration. Since the Hamiltonian is invariant to all rotations, the proper linear combinations of Slater determinants are those which correspond to definite values of \hat{L}^2 , \hat{L}_z , \hat{S}^2 , and \hat{S}_z , and the energy of such an L - S term, designated ^{2S+1}L , is independent of M_L and M_S . The terms differ in energy by intra-atomic Coulomb energies, i.e. eVs. The $(2L+1)(2S+1)$ -fold degeneracy of a term will be lifted by the SO coupling, in the presence of which L , S , J , and M_J , rather than L , S , M_L , and M_S , are good quantum numbers. Here J is the quantum number for the length of $\hat{J} \equiv \hat{L} + \hat{S}$. An atomic level is thus designated by the symbol $^{2S+1}L_{2J+1}$, and the levels of a given term form its *multiplet* structure.

For a given configuration the state of the lowest total energy usually follows from the three *Hund rules* which dictate that one should first choose the maximum value of S consistent with the Pauli principle, then the maximum value of L , and finally the minimum value, $|L - S|$, of J if the shell is less than half full, and the maximum value, $|L + S|$, of J if the shell is more than half full.

3 Band structures of the elemental metals

Referring to Walter Harrison's textbook [4] for a more comprehensive view, I shall concentrate on the elements in the left part of the periodic table. This part includes the one with d - and f -electron elements. They become either superconducting ("itinerant") or magnetic ("localized") at low temperature. A table reorganized in such a way that this separation becomes clearly visible and exhibits the elements of particular interest, namely those (Ce-Pr, Pu-Am, Mn-Fe, Rh-Co, Pd-Ni) around the border line, was reproduced as Fig. 1 in Richard Martin's lecture notes and discussed there [16].

3.1 Separating structure and potential

The structures of the alkali, alkaline earth, transition, noble, rare-earth, and most actinide metals are close- or closely packed with 12 (fcc, hcp, dhcp) or 8 (bcc) nearest neighbors at ambient temperature and pressure. The Wigner-Seitz (WS) cells are regular polyhedra with 12 or 8 faces and – as "seen" by an s -, p -, or d -electron with at most 4 orbital lobes – they are almost spherical, and so is the crystal potential, $V(\mathbf{r})$, inside a WS cell. If we approximate this potential by a superposition of spherically symmetric potential wells, $v(r)$, centered at the atomic sites: $V(\mathbf{r}) \approx \sum_{\mathbf{R}} v(|\mathbf{r} - \mathbf{R}|)$, each well can have short range. If we force it to vanish outside the sphere inscribed the WS cell, this forces the crystal potential to take the form of a muffin-tin (MT). Such potentials are used to generate the basis sets in the Korringa-Kohn-Rostocker (KKR) and (linear) augmented plane-wave (L)APW methods of band theory [5, 17]. By being able to handle slightly overlapping potential wells, muffin-tin orbitals (EMTOs, LMTOs, or NMTOs) are, individually, more accurate than APWs [18].

The full lines in Fig. 3 show $v(r)$ and $v_d(r)$ for the MT potential in fcc Pt, lined up near the nucleus with the weak lines showing those potentials in a neutral Pt atom. In elementary, closely-packed solids where the WS cells are neutral and nearly spherical, $v(r)$ bends over towards the value of the self-potential, $-2/s$, because the charge which in the neutral atom was outside the WS sphere is compressed into it [19]. Adding now the centrifugal repulsion, we see that $v_d(r)$ – rather than confining $\varphi_d(\varepsilon_{5d}, r)$ as in the atom – develops a barrier through which the $5d$ states in the solid can leak out, thus causing the atomic $5d$ -level to broaden into a band (cross-hatched). To understand the details of this, we need to consider how $\varphi_l(\varepsilon, r)$ depends on ε in the neighborhood of the atomic eigenvalue, ε_{nl} , as dictated by the radial equation (1) and the shape of $v_l(r)$. This is illustrated in Fig. 2 of Ref. [18]. The aim is to find the energies for which we can join linear combinations of partial waves, $\sum_{Rlm} \varphi_l(\varepsilon, r_R) Y_{lm}(\widehat{\mathbf{r}}_R) c_{Rlm}$ [notation: $\mathbf{r}_R \equiv \mathbf{r} - \mathbf{R}$ and $r_R \equiv |\mathbf{r}_R|$], with different lm and \mathbf{R} smoothly across the boundaries of the WS cells and thus form solutions of the Schrödinger equation for the solid. If it is a crystal with one atom per cell, the linear combinations in neighboring cells separated by a translation \mathbf{t} should merely differ by the Bloch phase $\exp(i\mathbf{k} \cdot \mathbf{t})$. This is how Wigner and Seitz posed the band-structure problem, but it proved difficult to solve in that way. However, the generalized WS rules, used in the renormalized-atom approach [19], stating that there will be a band of l -character extending

The matrix $S_{l'm',lm}(\mathbf{k})$ is the bare canonical structure matrix, which depends on the Bloch vector \mathbf{k} , but is independent of the energy and the scale of the lattice. Each diagonal block, $S_{lm',lm}(\mathbf{k})$, can be diagonalized, once and for all, yielding the so-called canonical bands, $S_{li}(\mathbf{k})$, which upon scaling via $P_l(\varepsilon)$ become the unhybridized l -bands, $\varepsilon_{li}(\mathbf{k})$. In Fig. 4 we show the ten canonical d -bands for the hcp structure with two atoms per primitive cell, the most common structure of the elemental metals. Obviously, the detail displayed here is way beyond the WS rules, which merely state that the l -band extends from $D_l = 0$ to $-\infty$, which rescales to P_l extending from $-2(2l+1)(l+1)/l$ to $2(2l+1)$, i.e., from -15 to $+10$ for the d -band, from -12 to $+6$ for the p -band, and from $-\infty$ to $+2$ for the s -band. This agrees surprisingly well with the more accurate values taken at the edges of the canonical bands, albeit less well in the more open bcc structure. This may be seen in Figs. 4 and 5, and in Refs. [8, 10–12]. The center of gravity of a canonical band, i.e., its first moment integrated over the Brillouin zone, is zero, and so is its average for any \mathbf{k} -point, except for the canonical s -band, and for the p -bands at $\mathbf{k}=\mathbf{0}$. Knowledge of the potential parameters, tables of which may also be found in Refs. [8, 10, 11] and with most detail in [12], allows one to construct the unhybridized energy bands by placing them at the respective energies, C_l , scaling them by, Δ_l , and distorting them by γ_l . Finally, the s -, p -, and d -bands belonging to the same irreducible representation (the numbers in Fig. 4) should be allowed to hybridize by taking the off-diagonal blocks of the structure matrix into account. This is illustrated in Fig. 6, but since the distortion of the s -band and its hybridization with the p -band are relatively large, thus developing into a nearly free-electron like sp -band, the unhybridized bands shown here were defined with respect to the *screened* structure matrix: $S^\gamma \equiv S[1 - \gamma S]^{-1}$. The quantities in this screening equation are matrices and γ is diagonal. In the γ -representation, the one-electron Hamiltonian takes the simple, orthogonal tight-binding form [12, 22]

$$H_{R'l'm',Rlm}^\gamma(\mathbf{k}) = \sqrt{\Delta_{R'l'}} S_{R'l'm',Rlm}^\gamma(\mathbf{k}) \sqrt{\Delta_{Rl}} + C_{R'l'} \delta_{R'R} \delta_{l'l} \delta_{m'm}. \quad (8)$$

For completeness we have included an index, R , labelling the sites, \mathbf{R} , of the atoms in the primitive cell. For the hcp structure considered in Fig. 4, the two sites are identical, so that the potential parameters are independent of R , but the dimension of structure matrix is doubled.

The ASA brought the realization that the bewilderingly complication of the band structures of d - and f -band materials is primarily of *structural* origin and can be expressed as canonical bands or hopping integrals. The *potential* and, hence, the approximations for exchange and correlation, merely decide the positions and widths of – and the hybridizations between – these s -, p -, d -, and possibly f -bands. This partly explained why a standard potential construction could work so well for Fermi surfaces and low-energy excitations [10, 23]. The original KKR method, *has* the form (6), but its structure matrix has long $|\mathbf{R}' - \mathbf{R}|$ -range end thereby depends strongly on energy so that obtaining the band structure, $\varepsilon_j(\mathbf{k})$, requires a complicated search for the roots of a secular determinant.

The insight leading to the ASA (6) was that the relevant energies, ε , are less than ~ 2 Ry above the potential, $-2/s$, in the region between the atoms (Fig. 3), whereby the corresponding wavelengths, $\lambda \equiv 2\pi/\kappa \gtrsim 2\pi/\sqrt{2}$ a.u., exceed typical interstitial distances in closely packed mate-

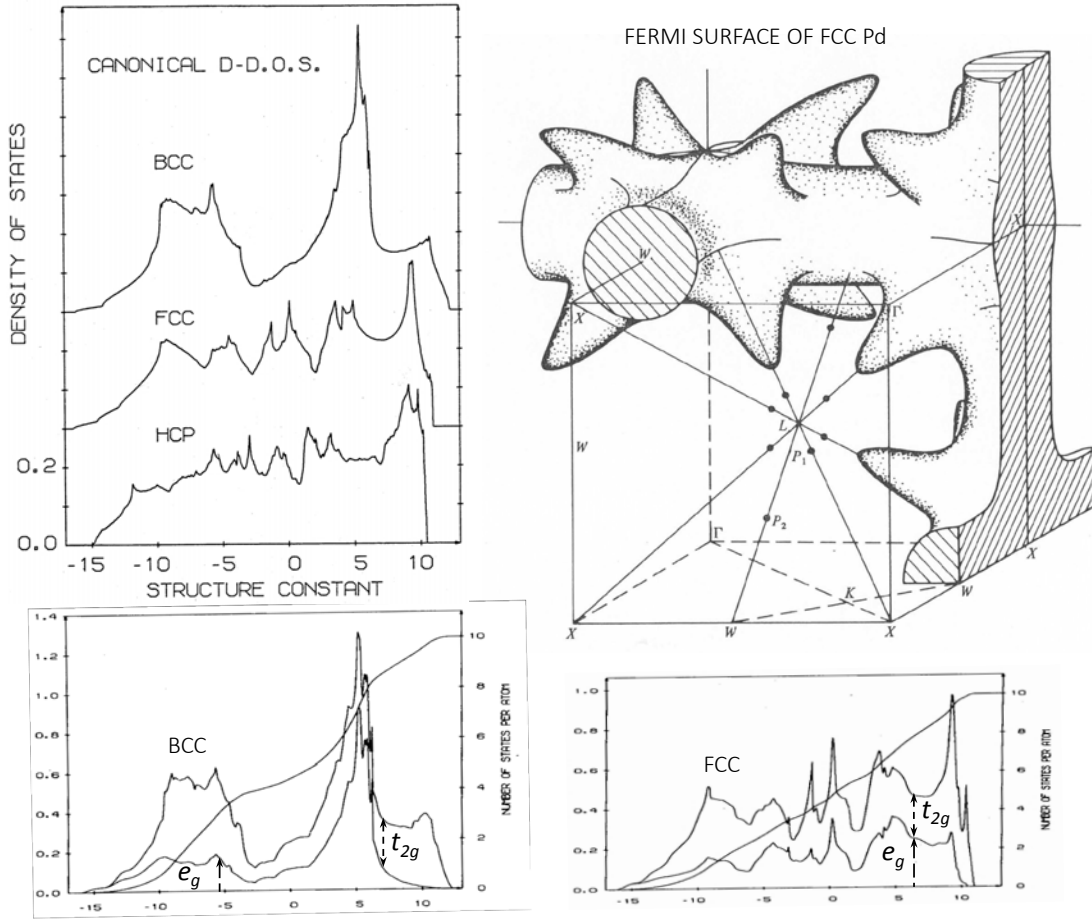


Fig. 5: Densities of states (DOS) for the bcc, fcc, and hcp ($c/a = \sqrt{8/3}$) bare canonical d-bands and their separation into e_g and t_{2g} projections for the bcc (bottom left) and fcc (bottom right) structures. From Ref. [8]. The open, heavy-hole FS-sheet in fcc Pd. The van Hove singularities caused by the saddlepoints in this 5th band at P_1 and P_2 , lying respectively 2 and 13 mRy below ε_F , bracket the large DOS peak at the top of the fcc d-bands. From Ref [15]. A tiny hole pocket (not shown) caused by spin-orbit splitting at L existed in the calculation and was observed later [21].

rials, and therefore need not be accurate. Similarly, partial waves with $l \lesssim 3$ cannot distinguish between touching and slightly overlapping MT spheres. The simplest choice was therefore to join a solution of the Laplace equation smoothly onto the partial wave at the WS radius:

$$\frac{\varphi_l(\varepsilon, r)}{\varphi_l(\varepsilon, s)} = \frac{D_l(\varepsilon) + l + 1}{2l + 1} \left(\frac{r}{s}\right)^l + \frac{l - D_l(\varepsilon)}{2l + 1} \left(\frac{r}{s}\right)^{-l-1}$$

and then subtract the function which is irregular at infinity

$$\chi_l(\varepsilon, r) \equiv \varphi_l(\varepsilon, s) \begin{cases} \frac{\varphi_l(\varepsilon, r)}{\varphi_l(\varepsilon, s)} - \frac{D_l(\varepsilon) + l + 1}{2l + 1} \left(\frac{r}{s}\right)^l & \text{for } r \leq s \\ \frac{l - D_l(\varepsilon)}{2l + 1} \left(\frac{r}{s}\right)^{-l-1} & \text{for } r \geq s \end{cases} \quad (9)$$

to obtain a regular function which decays as an electrostatic 2^l -pole field. This is essentially the 1st-generation MTO whose tail is trivial to expand around other sites, thus giving rise to

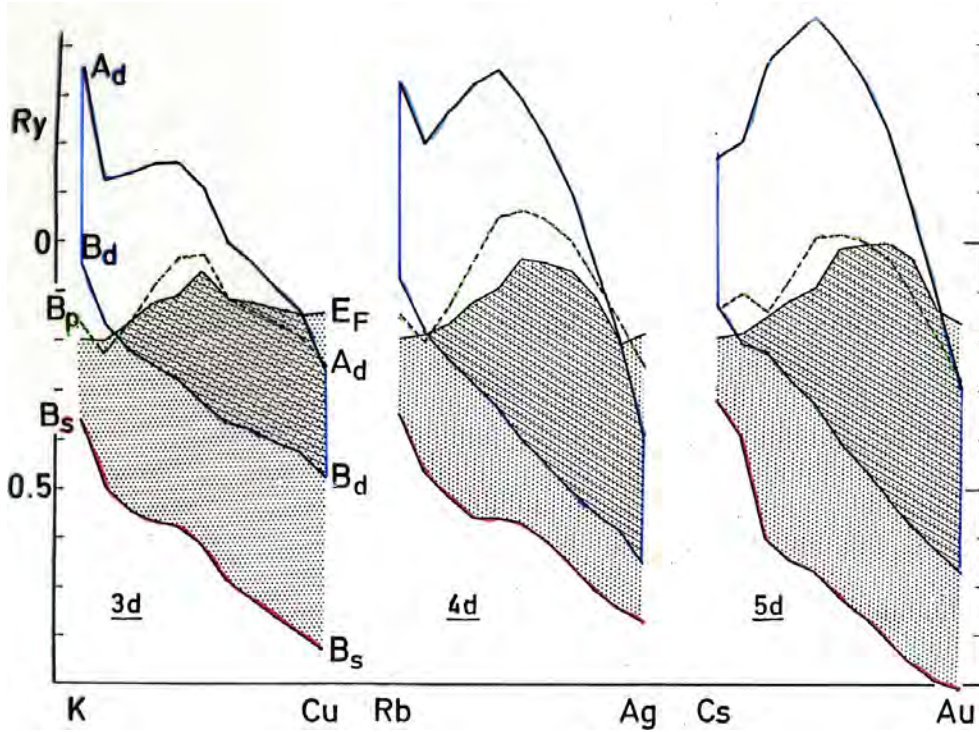


Fig. 7: Band edges in the elemental, close-packed $(n-1)d ns np$ metals. B_i bottoms of the s (red), p (green), and d (blue) bands. A_d (dark blue) top of the d band. E_F (black) Fermi level. The filled part of the sp and d bands are respectively dotted and cross hatched. The zero of energy is the electrostatic potential at the WS sphere. Lu rather than La was taken as the 3rd 5d metal. DFT-LDA and LMTO were used in the calculations. From Table III in Ref. [12].

elements (Figs. 1 and 2): First, and most dramatically, the filling of the ns band going from the alkalis to the alkaline earths causing B_s , B_p , and B_d to drop sharply and the ns orbital to contract. Subsequently, the gradual development of the $(n-1)d$ -band from being empty and free-electron like in the alkali- and alkaline earths, to being an occupied semi-core band beyond Cu, Ag, and Au, i.e., in Zn, Cd, and Hg. When going from the alkaline earths to the first transition metal, B_p and B_d move below the Fermi level, but while B_d and B_s continue to drop, B_p moves up again and more or less stays slightly above ε_F throughout the transition series. The shape and occupation of the nearly-free-electron $ns np$ -band thus stay fairly constant. The Fermi level follows a parabolic, downwards curving trend which results from the combined effects of filling-up the d -band and lowering its center of gravity. The internal work function, $-\varepsilon_F$, differs by the surface dipole from the external work function, which experimentally increases from 3.1 eV in Y to 5.5 eV in Pd, as an example, while $-\varepsilon_F$ merely increases by 0.4 eV from 2.3 to 2.8 eV. The experimental ionization potential for atoms shown in Fig. 2 increases from 6.5 to 8.5 eV [26].

Included in the LDA energies in Fig. 7 is the solid-state effect that the filling of first the ns - and then the $(n-1)d$ -bands causes the lattice to contract (Fig. 8) and this, itself, causes the bands to broaden. The broadening is most visible for the d -bands whose bandwidth, $A_d - B_d = 25\Delta_d$, and reaches its maximum at respectively V, Nb, and Ta. Going from one period to the next,

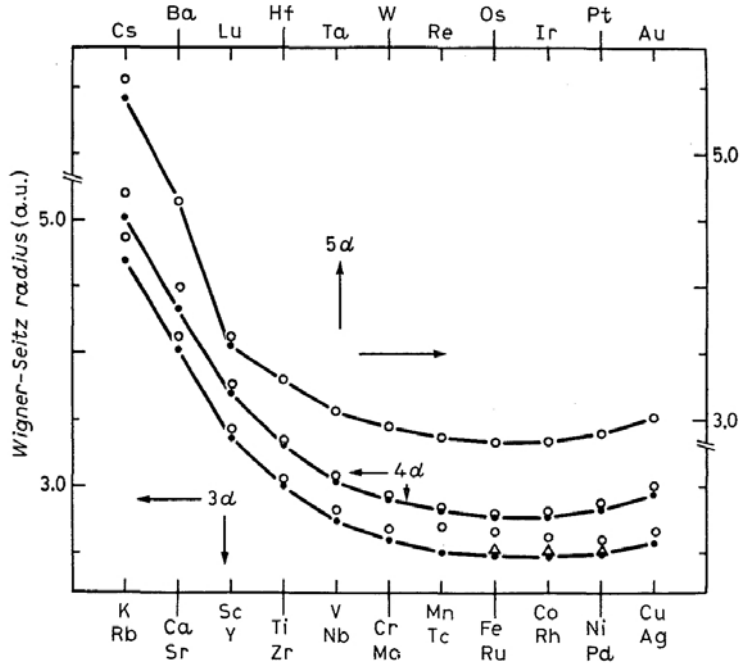


Fig. 8: Equilibrium WS radii for the elemental alkali, transition, and noble metals. Open dots are the experimental values. The line and the full dots are the results [12] of LDA LMTO [14,26] calculations. The open triangles are LSD calculations for Fe, Co, and Ni. From Ref. [12].

i.e., increasing n , makes the orbitals expand and with them, the lattice and the bandwidths. Now, the energy of an electron, free with respect to a flat potential V_s ($\equiv B_s$) is purely kinetic, and its band therefore scales like s^2 . In Fig 9, we therefore plot for the $4d5sp$ series the filled free-electron bandwidth $s^2(\varepsilon_F - V_s)$, which is seen to be more constant than ε_F in Fig. 7. The $s^2(C_d - V_s)$ -measure of d -band position, together with the inverse of the mass at the center of the d -band, Eq. (11), clearly exhibit the drop and narrowing of the d -band with respect to the sp -band. Fig. 9 finally shows the behavior of the square-well pseudopotentials V_l , and the inverse of the band masses, τ_l , at the respective V_l

$$\frac{1}{\mu_l} \equiv s^2 \Delta_l = \frac{1}{2} s^3 \varphi_l^2(C_l, s) \quad \text{and} \quad \frac{1}{\tau_l} = \frac{1}{2l+3} s^3 \varphi_l^2(V_l, s). \quad (11)$$

These inverse masses are proportional to the respective probability amplitudes at the WS sphere, i.e., between the atoms. Since the partial waves are normalized to unity in the WS sphere, this means that, had the partial wave been as in the atom, the band mass would be proportional to the (re)normalization integral over the WS sphere [19]. The bottom of the $5s$ -band lies well above the $4f$ -pseudopotential which, itself, is close to the potential $\sim -2/s$ at the WS sphere. Moreover, the $5s$ -mass is significantly smaller than unity and attains a minimum, as do $(V_f - V_s) s^2$ and $(-2/s - V_s) s^2$, near the middle of the series. This means that the $5s$ -electron is excluded from the core region (orthogonalization hole). For a further discussion of this point and other trends in the $4d5sp$ series see Ref. [9].

The relativistic corrections (4) originate close to the nuclei and are negligible between the atoms. But this does not mean that their effects in solids are the same as in atoms: In the ASA we may, initially, normalize the solution, $\varphi_l(\varepsilon, r)$, of the radial equation to have the same behavior

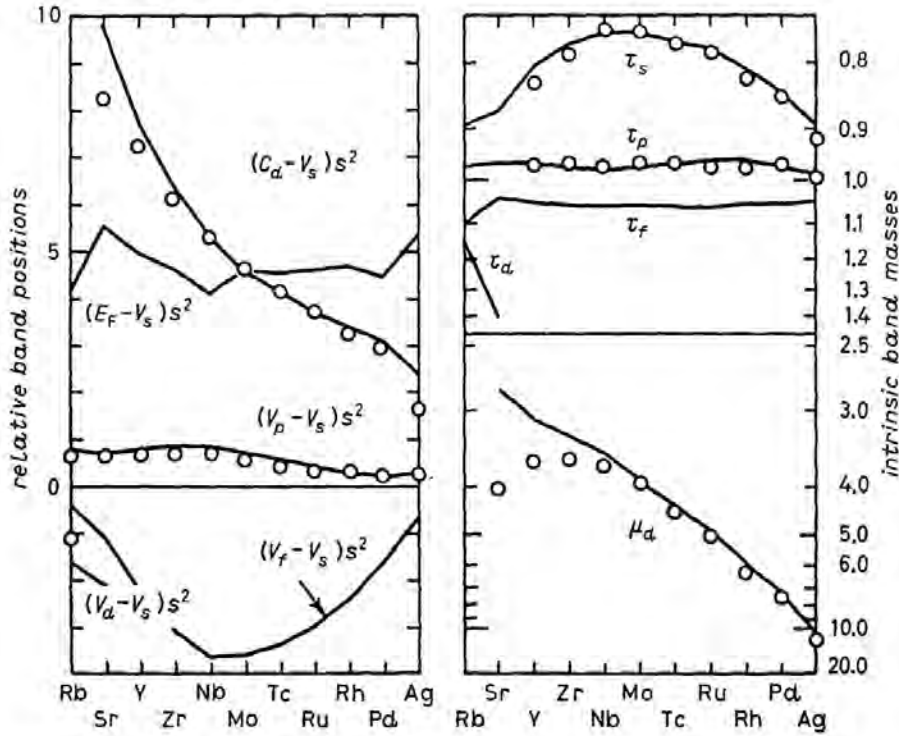


Fig. 9: Band positions relative to the bottom of the s -band, $B_s=V_s$, in dimensionless units, and intrinsic band masses, τ_l and μ_d , on a reciprocal scale, in the $4d$ $5sp$ -series; see text. Open circles from the Mattheiss-Slater [27] construction (from Ref. [8]) and full lines from the LDA [26] (from Ref. [10, 12]). For Rb, Sr, and Ag, the LDA yield Fermi surfaces in better agreement with experiments.

near a given nucleus, i.e., integrate the radial equation outwards with the same initial condition regardless of the surroundings and the energy. In the solid, $\varphi_l(\varepsilon, r)$ must then be (*re*)normalized to inside the WS sphere [see, e.g., Eq. (11)], and this makes the magnitudes of the relativistic effects *larger* in the solid than in the atom by a factor of approximately $1/(1 - q_{nl})$, where q_{nl} is the fraction of the *atomic* nl -electron which lies outside the WS sphere. This fraction is about 0.5 for s -electrons and less than 0.1 for d -electrons. The partial-wave renormalization furthermore causes the magnitude of the relativistic effects in the solid to increase from the bottom (B_l) to the top (A_l) of the band, and this increase is nearly a factor two! The width of the l -band is thereby decreased by the relativistic shifts, but increased by the SO splitting. When going beyond the ASA, such renormalization effects are described by the overlap of the MTOs (see Fig. 3 in Ref. [18]).

Of the relativistic corrections, the shifts are the most important and they have been included in, e.g., Figs. 7 and 9. The downwards shift of the center of the ns -band (due to the mass-velocity minus Darwin terms) with respect to the center of the $(n-1)d$ band (due to mass-velocity), $C_{ns} - C_{(n-1)d}$, is about 15 mRy, 75 mRy, and 250 mRy in the middle of the $3d$ -, $4d$ -, and $5d$ -series, respectively. As a result, the number of non- d -electrons increases from 1.50 ± 0.10 e/atom in the $3d$ - and $4d$ -series to 1.75 ± 0.15 in the $5d$ -series. Here, the smaller/larger number refers to the beginning/end of the series. Note also that the bottom, B_p , of the p -band is occupied in the second half of the $3d$ - and $5d$ -, but not in the $4d$ -series.

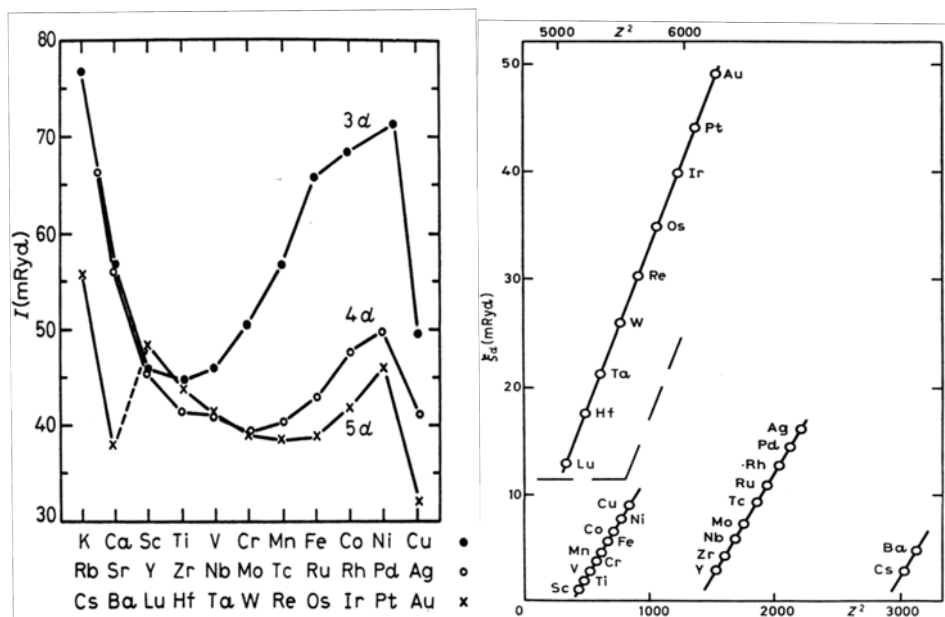


Fig. 10: Left: LSD [26] Stoner parameter, I , at ε_F calculated [12] with the LMTO method and using the procedure of Janak [28]. Right: Spin-orbit coupling parameter ξ_d (C_d) for the center of the d -band in elemental transition metals as a function of Z^2 . Note that $\xi_d(\varepsilon)$ increases by about a factor 2 from the bottom to the top of the d -band. From Ref. [12].

The SO coupling parameters shown in Fig. 10 are typically one order of magnitude smaller than the relativistic shifts. Moreover, for crystals with inversion symmetry, the SO coupling cannot split the two spin bands and therefore gives rise to splittings of first order in ξ only in small regions of k -space near points of degeneracy. SO coupling is important near the top of the d -bands where the bands have t_{2g} character (see Fig. 5).

The abrupt increase in the size of the relativistic effects seen in Figs. 7 and 10 between the 2nd (Ba) and 3rd (Lu) $5d$ -elements is caused by the jump of Z due to the insertion of the 14 Lanthanides. All of those are, contrary to the case for the atoms (Fig. 1), trivalent $5d$ -metals ($4f^n 5d^1 6s^2$) with the exceptions of divalent Eu ($4f^7 6s^2$) and Ce ($4f^x 5d^{2-x} 6s^2$), whose α - γ transition was discussed by Richard Martin in last year's lecture notes [16]. In this connection it should be mentioned that the actinides are $5f^n 6d^1 7s^2$ -metals whose $5f$ -electrons are itinerant in the first- and localized in the second part of the series.

In the 60ies and 70ies, energy bands computed using the standard, non-selfconsistent, Mattheiss-Slater construction of the crystal potential [27] were found to give surprisingly good agreement between experimental and computed Fermi surfaces, and useful optical spectra for nearly all elemental metals in the $4d$ - and $5d$ -series [10]. When in the late 70ies and early 80ies it became possible to perform selfconsistent DFT calculations [9, 10, 29–31], it turned out that one and the same local exchange-correlation potential [26] not only gave “bastard” bands which were nearly identical with those obtained with the Mattheiss-Slater construction (see Fig. 9), but also gave what DFT was designed for: good total energies, or rather: good total-energy differences, e.g., lattice constants, structures, trends, and last, but not least, Car-Parrinello molecular dynamics [10, 12, 31–33]. Towards the end of the 80ies DFT was accepted in a large part of the condensed-matter community and rapidly spreading beyond [23].

3.2 Force theorem, pressures, and structures

The cohesive properties (at $T=0$) can be computed from the total-energy. But this provides little insight, because it is expressed in terms of largely cancelling quantities, the selfconsistently calculated Coulomb energies of the electron-electron and proton-proton repulsions and of the electron-proton attraction, plus the kinetic energy of the electrons. However, the cohesive properties only involve total-energy *differences* and these are given to *first* order by the difference of the one-electron energies calculated for *frozen* one-electron potentials (i.e., the difference of kinetic energies avoids double counting of the e-e interactions) plus the difference of Madlung energies. This so-called force theorem was originally proved within the LDA in Refs. [10, 34, 35]. With appropriate definitions it holds in general, but only to 1st order [36].

In the following, I shall illustrate this by application to pressure-volume relations and crystal structures of the closely-packed elemental metals.

3.2.1 Partial pressures

Neglecting the zero-point motion of the nuclei, the pressure, \mathcal{P} , which must be applied in order to keep the crystal in equilibrium at a given volume, \mathcal{V} , is the change of the total energy with uniform compression (see top left part of Fig. 11). In terms of the equation of state, $\mathcal{P}(\mathcal{V})$, the equilibrium atomic volume, $\mathcal{V}_0 = (4\pi/3) s_0^3$, is determined by $\mathcal{P}(\mathcal{V}_0) = 0$, the bulk modulus by $\mathcal{B} = -d\mathcal{P}/d\ln\mathcal{V}|_{\mathcal{V}_0}$ and the cohesive energy per atom by

$$E_{\text{coh}} = - \int_{\mathcal{V}_0}^{\infty} \mathcal{P} d\mathcal{V} = - \int_{s_0}^{\infty} 3\mathcal{P}\mathcal{V} d(\ln s),$$

where s_0 is the equilibrium WS radius. With the force theorem, the pressure is most conveniently calculated by “peeling the skin off” the self-consistent, cellular potential, moving the frozen potentials together in the compressed structure, and recalculating the sum of the one-electron energies. To the change of the latter, should finally be added the change of electrostatic energy between the cells. I.e.

$$3\mathcal{P}\mathcal{V} \equiv - \frac{dE_{\text{tot}}}{d\ln s} = - \sum_{i\mathbf{k}}^{\text{occ}} \frac{\delta\varepsilon_i(\mathbf{k})}{\delta\ln s} - \frac{\delta\text{Mad}}{\delta\ln s}, \quad (12)$$

where δ indicates the derivative for frozen potentials in the first term and frozen charge densities in the second [36]. For closely-packed elemental solids, the latter may often be neglected so that only the one-electron energies remain.

In the ASA (6), only the logarithmic-derivative functions (5) change because they must be re-evaluated at an infinitesimally smaller WS radius. What happens to the band edges, B_l and A_l , may be understood from the bottom left part of Fig. 11, where the bonding and antibonding partial waves, $\varphi_l(B_l, r)$ and $\varphi_l(A_l, r)$, are shown for cases where B_l and A_l lie above the value $v_l(s)$ of the effective potential at the sphere (dotted) and where they lie below (full) [see Fig. 3]. In the dotted case, the region between the atoms is classically allowed so that, according to the radial Schrödinger equation (1), $r\varphi_l(\varepsilon, r)$ curves towards the r -axis, whereas in the full,

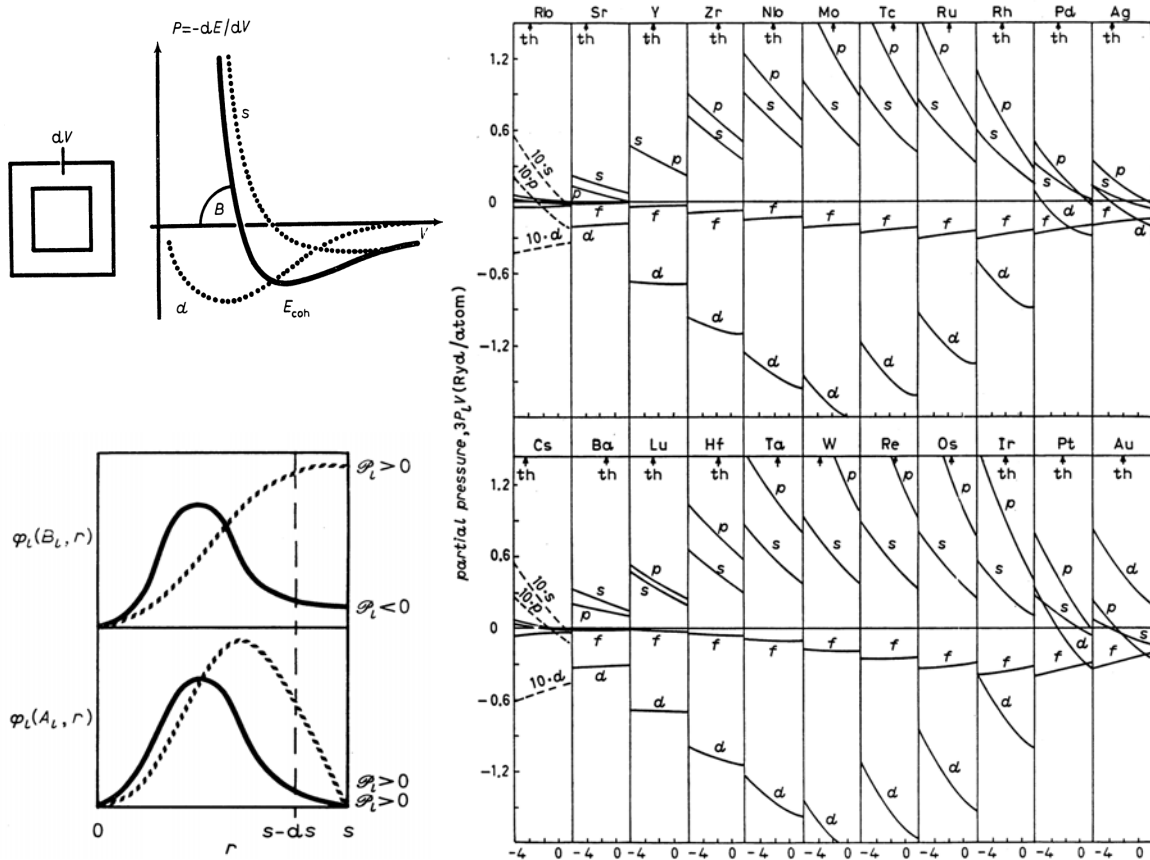


Fig. 11: Top left: Total and partial pressure-volume curves (schematic). The bulk modulus is the slope of the curve, the equilibrium volume is the intersection with the volume axis, and the cohesive energy is the area below the curve from the intersection to infinity. Bottom left: Radial wave functions (normalized for $r \rightarrow 0$), $\varphi_l(r)$, at the bottom (B_l) and top (A_l) of the l -band. The dotted/full lines are for cases where B_l and A_l are above/below the effective potential, $v_l(s)$, at the WS sphere. The sign of the partial pressure, \mathcal{P}_l , is indicated. Right: Partial pressures calculated with LDA LMTO [12] for the $5sp4d$ and $6sp5d$ series as functions of the percentage deviation from the experimental WS radius at zero pressure. The calculated deviations are indicated by “th”. From Ref. [12].

classically forbidden case, $r\varphi_l(\varepsilon, r)$ curves away from the axis and the electron must tunnel out of the WS sphere in order to get to a neighboring atom.

Now, under compression we need to re-install the bonding/antibonding boundary conditions at $s-ds$ and to use the fact proved below Eq. (7), that the logarithmic derivative is an ever-decreasing function of energy. From Fig. 11 we see that if s is classically allowed, the slope $\varphi'_l(B_l, s-ds)$ is positive, so that in order to re-install the zero-slope condition, we must increase the energy, i.e., the bottom of the l -band goes up upon compression, and this means that it adds to the pressure, $\mathcal{P}_l(B_l)$, i.e., will tend to press the nuclei apart. This is the case for electrons in bonding states at the bottom of broad bands such as s and p , because their centrifugal repulsion vanishes, or is small, and because the bandwidth is proportional to $[-dD_l(\varepsilon)/d\varepsilon]^{-1} = s\varphi_l^2(\varepsilon, s)/\langle\varphi_l^2(\varepsilon)\rangle$, the probability of being at the sphere. If, on the other hand, the interstitial

region is classically forbidden, $\varphi'_l(B_l, s - ds)$ is negative and the bottom of the l -band therefore goes down in energy upon compression. Its contribution to the pressure is negative, i.e., the *bonding electrons at the bottom of narrow bands* are attractive, they tend to keep the nuclei together. This is the case for transition-metal d -bands. At the top of an l -band, the slope $\varphi'_l(A_l, s - ds)$ is always negative, so that in order to re-install the $\varphi_l(A_l, s) = 0$ condition, we must always increase the energy, and this means that the antibonding electrons at the top of an l -band are always repulsive, i.e., press the nuclei apart.

The right-hand side of Fig. 11 shows for the metals in the $4d$ - and $5d$ -series the partial pressures as functions of the percentage deviation of s from the experimental low-temperature values. The values where the total pressure vanishes, the theoretical WS radii, are indicated by arrows. The experimental and theoretical absolute values were shown in Fig. 8. The picture of the bonding emerging is that the d -electrons contract the crystal against the repulsion from the “more free” sp -electrons. This attraction increases until the bonding states in the lower part of the d -band are full and filling of the antibonding states in the upper part starts. In Au, the d -electrons are seen to be repulsive (hard core repulsion) while in Ag, they are still attractive. We also note that the bulk moduli in the $6sp5d$ -series are larger than those in $5sp4d$ -series. Had it been possible to decompose the pressures according to an spd -set of local orbitals, rather than partial waves, the small attractive f -pressures would have been associated with the tails of these orbitals.

The ASA pressure relation was originally derived from the virial theorem and we can get to the form given by Pettifor [37] by using the radial Schrödinger equation (1) to express the derivative, $\delta D_l(\varepsilon)/\delta \ln s$, of the logarithmic-derivative function (5) as

$$-s \left(\frac{s \varphi'}{\varphi} \right)' = -s \frac{(s \varphi)''}{\varphi} + \frac{s \varphi'}{\varphi} + \left(\frac{s \varphi'}{\varphi} \right)^2 = (\varepsilon - v_l(s)) s^2 + D(\varepsilon) (D(\varepsilon) + 1).$$

Note in passing, that since $D_l(D_l + 1) = (D_l + l + 1)(D_l - l)$, the contribution to the pressure by not only electrons at the bottom, B_l , but also at the center, C_l , of the band, and at the energy, V_l , of the square-well pseudopotential is proportional to $\varepsilon - v_l(s)$. Now, the energy, $\varepsilon_l(D)$, corresponding to the boundary condition D at s , i.e., the function inverse to $D_l(\varepsilon)$, is

$$-\frac{\delta \varepsilon_l(\varepsilon)}{\delta \ln s} = -\frac{\delta D_l(\varepsilon)}{\delta \ln s} \left(\frac{dD_l(\varepsilon)}{d\varepsilon} \right)^{-1} = \left((\varepsilon - v_l(s)) s^2 + (D_l(\varepsilon) + 1) D_l(\varepsilon) \right) s \varphi_l^2(\varepsilon, s)$$

where $\varphi_l(\varepsilon, r)$ is normalized to 1 in the WS sphere. Multiplication by the l -projected DOS and integration up to the Fermi level yields Pettifor's pressure relation. The form (12) is more intelligible and, using the Hamiltonian (8) or the full LMTO version, requires the $\delta \ln s$ -derivatives of the potential parameters given analytically in, e.g., Ref. [12].

3.2.2 Structures

The structural sequence for the non-magnetic transition metals at low temperature and ambient pressure is: hcp (Sc, Y, Lu), hcp (Ti, Zr, Hf), bcc (V, Nb, Ta), bcc (Cr, Mo, W), hcp (Tc, Rs), hcp (Ru, Os), fcc (Rh, Ir), and fcc (Ni, Pd, Pt). Already in the late 60ies [39], it had been pointed out that this reflects a trend in the sum of the one-electron energies, but the force theorem made the

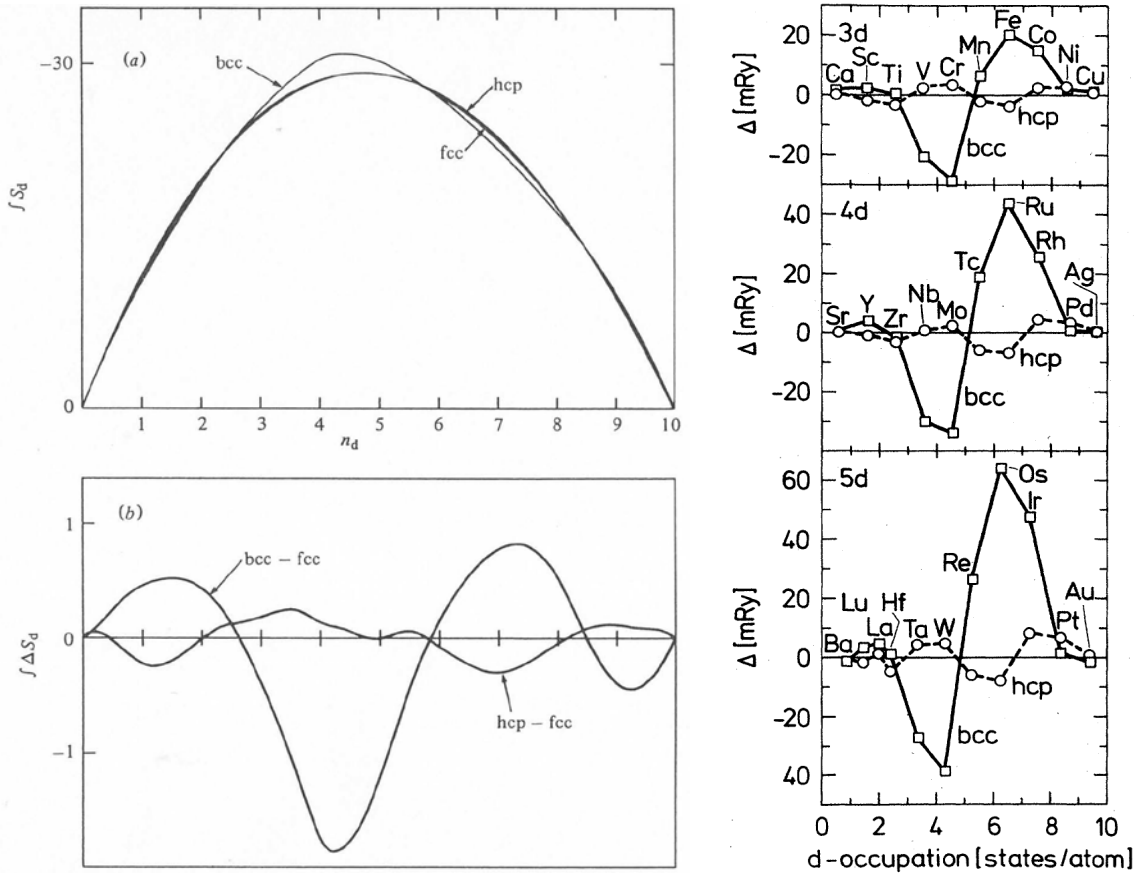


Fig. 12: Left: (a) First moment of the canonical d -band density of states in Fig. 5 as function of its occupancy, n_d . Note that negative values are upwards so that the curve resembles that of the cohesive energy. (b) The bcc-fcc and hcp-fcc structural differences, now with positive moments upwards. From Refs. [30, 10]. Right: Structural energy differences calculated by LDA-LMTO for the $4sp\ 3d$, $5sp\ 4d$ and $6sp\ 5d$ series at the experimental equilibrium volumes and plotted as functions of the calculated number of d -electrons. From Ref. [38].

computational procedure accurate and more generally applicable. Now, if we assume that the difference between the closely-packed structures, at conserved atomic volume, is a 1st-order effect, we can use the force theorem with the same atomic-sphere potential in all structures, and if we use the ASA, the Madelung energy vanishes because the spheres are neutral. If we finally neglect the s - and p -bands and consider merely the bare, canonical d -bands, the structural energy difference in units of Δ_d is simply the difference between the 1st canonical moments,

$$\int^{S(n_d)} S N_d(S) dS, \quad \text{with } n_d \equiv \int^{S(n_d)} N_d(S) dS,$$

shown to the left in Fig. 12 as a function of the number, n_d , of bare, unhybridized d -electrons per atom. The canonical densities of states, $N_d(S)$, were shown in Fig. 5 and $S(n_d)$ is the canonical Fermi level. As mentioned before, the 1st moment of a bare canonical band always vanishes when the band is full. Had $N_d(S)$ in Fig. 5 been rectangular, the first moment would have been a parabola resembling the behavior of the cohesive energy as a function of the d -band filling [40]. But now, the structural differences shown at the bottom of Fig. 12 clearly reproduce the observed

structural sequence. The characteristic two-peak structure in the bcc DOS, makes this structure stable for materials with the Fermi level in the gap between the peaks. By properly including the s - and p -bands and the hybridization with them, as well as the Madelung- and the so-called combined-correction to the ASA, i.e., by doing proper LDA-LMTO calculations, Skriver [38] obtained the results shown in the right-hand panel. Independent, exhaustive LAPW total-energy calculations [41] for merely bcc and fcc Cr, Mo, and W agree within 2 mRy with Skriver's results, thus confirming his approach. But also the ten-times-smaller energy differences between the hcp and fcc metals, having merely different stackings along (111) and, hence, $N_d(S)$ -shapes, give structures in agreement with experiments. Skriver also considered La, Ce, and Lu, as well as Th and Pa. In fact, of the 39 non-magnetic cases studied, only for Na, Au, Yb, and Pa, the correct structure was less stable than the one calculated.

Using the same methodology as Skriver, McMahan and Moriarty studied the pressure-induced phase transitions between the closely-packed structures of Na, Mg, Al, and Si, and found these transitions to be driven by the hybridization of the occupied sp -bands with the bottom of the $3d$ -band moving down with pressure. Earlier, and in a similar way, Duthie and Pettifor [42] had explained the Lanthanide structural sequence: hcp, Sm-type, double-hcp, fcc, observed for decreasing atomic number and increasing pressure as a result of the increasing population of the falling $5d$ -band.

3.3 Band magnetism

The generalization of DFT to a spin-DFT [26, 43] was a first step in “helping” the density functional, through symmetry breaking, to treat exchange and correlation more accurately than in the LDA, which merely uses the xc-energy density, $\epsilon_{xc}(\rho)$, calculated for the homogeneous electron gas as a function of its density. In spin-DFT, the independent variable is the space-diagonal matrix element of the first-order density matrix, $\rho(\mathbf{r}\sigma, \mathbf{r}\sigma')$, and the self-consistency condition for the one-electron potential in the Schrödinger equation, which generates the density as:

$$\rho(\mathbf{r}\sigma, \mathbf{r}\sigma') \equiv \sum_k \theta(\epsilon_F - \epsilon_k) \psi_k^*(\mathbf{r}\sigma) \psi_k(\mathbf{r}\sigma'), \quad (13)$$

is given by

$$V(\mathbf{r}\sigma, \mathbf{r}\sigma') = V_{\text{ext}}(\mathbf{r}\sigma, \mathbf{r}\sigma') + V_C(\mathbf{r}) + V_{xc}(\mathbf{r}\sigma, \mathbf{r}\sigma'). \quad (14)$$

Here, V_{ext} is the Coulomb potential of the protons plus an external spin-dependent potential, such as: $-\text{sgn}(\sigma)\mu_B\mathcal{H}$ with $\text{sgn}(\uparrow) = \pm$, from a uniform magnetic field, V_C is the classical Coulomb potential from all electrons, and $V_{xc}(\mathbf{r}\sigma, \mathbf{r}\sigma')$ is the exchange-correlation potential. In case the potential (14) has translational symmetry, the state-label k is $i\mathbf{k}$. The density generated self-consistently from this potential minimizes the total-energy functional.

In its local approximation (LSD), spin-DFT uses $\epsilon_{xc}(\rho_\uparrow, \rho_\downarrow)$ for a homogeneous electron gas subject to a homogeneous magnetic field which creates a density, $\rho = \rho_\uparrow + \rho_\downarrow$, and a spin density, $m = \rho_\uparrow - \rho_\downarrow$. The corresponding exchange-correlation potential is diagonal in spin and equals $\partial(\rho \epsilon_{xc}(\rho_\uparrow, \rho_\downarrow))/\partial\rho_\sigma \equiv \mu_{xc\sigma}(\rho_\uparrow, \rho_\downarrow)$. Expansion around the non spin-polarized values, $\rho_\uparrow = \rho_\downarrow = \rho/2$, i.e., in powers of m yields $\epsilon_{xc}(\rho_\uparrow, \rho_\downarrow) = \epsilon_{xc}(\rho) + \epsilon_{xc}''(\rho) m^2/4 + \mathcal{O}(m^3)$, and,

hence, for the exchange-correlation potential

$$\mu_{xc\uparrow\downarrow}(\rho, m) = \mu_{xc}(\rho) \pm m \rho \epsilon''_{xc}(\rho)/2 + \mathcal{O}(m^2). \quad (15)$$

Here, μ_{xc} and $\epsilon''_{xc}(\rho)$ are both *negative*, so that increasing $m = \rho_{\uparrow} - \rho_{\downarrow}$ lowers the potential seen by a \uparrow -electron and rises it for a \downarrow -electron, i.e., exchange tends to align the spins. This leads to Hund's 1st rule for degenerate levels (an open shell) in atoms and since the Pauli principle prevents multiple occupation, level-separation works against spin-polarization.

3.3.1 Ferromagnetism

For a para- or ferromagnet (without SO coupling) in the presence of a uniform magnetic field, which provides the Zeeman splitting $\pm\mu_B\mathcal{H}$, the band-structure problem decouples into separate Schrödinger equations (14), one for each direction of spin. By filling the states to a common Fermi level (13) and solving selfconsistently, the zero-temperature spin-magnetizations, $m = \langle m(\mathbf{r}) \rangle$, the uniform susceptibilities, $\mu_B dm/d\mathcal{H}$, and magnetic contributions to the cohesive properties may be computed [30].

This was done in the mid-70ies using the ASA [29] and the results were interpreted in terms of Stoner theory with the exchange constant, I , obtained from the Stoner equation: $C_{d\downarrow} - C_{d\uparrow} = mI + 2\mu_B\mathcal{H}$ using the computed magnetization and splitting of the centers of the d -bands. Gunnarsson [44] used the spin-splitting of the xc-potential to order m in Eq. (15) and treated it by 1st-order perturbation theory on top of the paramagnetic bands. Hence, the band-splitting is

$$\varepsilon_{j\downarrow}(\mathbf{k}) - \varepsilon_{j\uparrow}(\mathbf{k}) = \langle \psi_{j\mathbf{k}}(\mathbf{r}) | -\rho(\mathbf{r}) \epsilon''_{xc}[\rho(\mathbf{r})] m(\mathbf{r}) | \psi_{j\mathbf{k}}(\mathbf{r}) \rangle + 2\mu_B\mathcal{H} \approx mI + 2\mu_B\mathcal{H}. \quad (16)$$

In the last approximation, the $j\mathbf{k}$ -dependence of I was neglected. Janak [28] evaluated I from essentially the same expression with the expectation value taken as the average over the paramagnetic Fermi surface. This is appropriate when subsequently filling the exchange-split bands (16) to a common Fermi level in order to get, first, the magnetization and, then, the splitting, $m/N(\varepsilon_F)$, by dividing m by the paramagnetic DOS per spin. Equating this splitting with the approximation (16), yields Stoner's expression for the exchange-enhanced spin-susceptibility

$$\chi \equiv \mu_B m / \mathcal{H} = 2\mu_B^2 N(\varepsilon_F) \left(1 - IN(\varepsilon_F)\right)^{-1}. \quad (17)$$

The values of I obtained for Fe, Ni, Rh, Ir, Pd, and Pt from LSD ASA calculations of $C_{d\downarrow} - C_{d\uparrow}$ [29,30] and from approximation (16) agree within a few percent. The trends apparent in Fig. 10 were explained by Gunnarsson [44] for the late transition metals plus V, and by Janak [28] for the entire $3d$ and $4d$ series, although in considerably less detail. The dominating trend that I decreases with increasing Z and, hence, with increasing ρ , is due to ϵ_{xc} being dominated by $\epsilon_x \propto \rho^{1/3}$, so that the kernel behaves like $-\rho \epsilon''_x \propto \rho^{-2/3} = (4\pi/3)^{2/3} r_s^2$, which decreases with ρ . For understanding that in a given series, I rises again until it drops sharply at the noble metals, we use the ASA, i.e., take $-\rho(\mathbf{r}) \epsilon''_{xc}[\rho(\mathbf{r})]$ and $m(\mathbf{r})$ to be spherically symmetric, and

expand $\psi_{j\mathbf{k}}(\mathbf{r})$ on the FS in partial waves. Since only partial waves with the same l contribute to I as defined in (16), we get

$$I \sim s \int_0^1 (r_s(r)/r)^2 \left(\alpha (r\varphi_{sp}(\varepsilon_F, r))^2 + (1 - \alpha) (r\varphi_d(\varepsilon_F, r))^2 \right)^2 d(r/s), \quad (18)$$

leaving out constants and using ϵ_x instead of ϵ_{xc} .

The form (18) with $\alpha = 0$ is the one discussed by Gunnarsson for the transition metals [44]. He showed that the factor $(r_s(r)/r)^2$, apart from its general decrease with Z , for Z given and r increasing, increases outside the last core np -shell, i.e., for $r \gtrsim 0.3s$, and peaks for $r \sim 0.8s$. This peaking is the combined result of the general increase of $r_s(r)$ with r and the filling of the nd -shell, whose charge-density peaks for $r \lesssim 0.5s$. One factor $(r\varphi_d(\varepsilon_F, r))^2$ in (18) comes from $|\psi_{j\mathbf{k}}(\mathbf{r})|^2$ and the other from $m(\mathbf{r})/m$. The product, $(r\varphi_d(\varepsilon_F, r))^4$, is very strongly peaked at a value $r \lesssim 0.5s$, which moves towards the edge of the np -shell as the Fermi level moves towards the top, A_d , of the d -band (Fig. 7) where $(r\varphi_d(A_d, r))^4$ vanishes smoothly for r approaching s . This behavior of the integrand $(r_s(r)/r)^2 (r\varphi_d(\varepsilon_F, r))^4$ explains the increase of I through the second half of a transition series (Fig. 10).

Prior to the filling of a d -shell, i.e., for the alkali-, alkaline-earth, and rare-earth metals, $(r_s(r)/r)^2$ merely increases monotonically with r , once it is outside the core, and its value at the WS sphere is approximately given by $nr_s^3(s) = 1$, where $n = 1, 2, 3$ is the number of valence electrons (Fig. 19 in Ref. [12]). The contribution to I of the sp -electrons is taken care of in Eq. (18) by $\alpha \equiv N_{sp}(\varepsilon_F) (N_{sp}(\varepsilon_F) + N_d(\varepsilon_F))^{-1}$, the relative sp -character on the Fermi surface. For $n_{sp} = n = 1$ and 2, the factor $(r\varphi_{sp}(\varepsilon_F, r))^4$, is the only one relevant, and it is fairly constant in the outer part of the WS sphere. The decrease of I for n increasing from 1 to 2, thus follows the factor- $2^{-2/3}$ decrease of $r_s^2(s)$. How, upon entering a transition series, this decreasing trend is taken over by the increasing trend at the end of the series, is described by Eq. (18) with α decreasing from 1 to 0 and $r_s(r)$ developing the above-mentioned d -peak. Finally, the relatively low I -values for the noble metals is due to the sp -character on the FS jumping from about 10 to 50% for Cu and Ag, and to 70% for Ag.

If we use the approximate Stoner equation (16) for a ferromagnet, the condition for spin self-consistency is that the integral over the paramagnetic DOS (per spin) over the energy range $mI + 2\mu_B\mathcal{H}$ equals the magnetization m . Since the number of electrons, $n_\uparrow + n_\downarrow$, must be kept constant, $m/2$ spins must be moved from above the paramagnetic Fermi level, ε_F , to below. This is illustrated in the left-hand panel of Fig. 13 using the unhybridized, canonical bcc d -DOS shown in Fig. 5, which is a good approximation for the d -projected DOS, $N_d(\varepsilon)$, in paramagnetic bcc Fe (see Fig. 7 in Ref. [8]). Insight to the workings of this self-consistency condition is provided by the construction from $N_d(\varepsilon)$ of a function, $\bar{N}(n, m)$, which is the DOS per spin, averaged around the Fermi level corresponding to an occupancy of $n/2$ spins, over a range corresponding to m spins. I.e.: for an assumed m , we move the Fermi level up and down in the rigid DOS until the integral is respectively increased and decreased by $m/2$. With Δ being the splitting between these two Fermi levels, $\bar{N}(n, m) \equiv m/\Delta$. This band-structure function is shown as a function of m at the bottom. Since, for paramagnetic Fe where $n_d=6.5$, ε_F is a

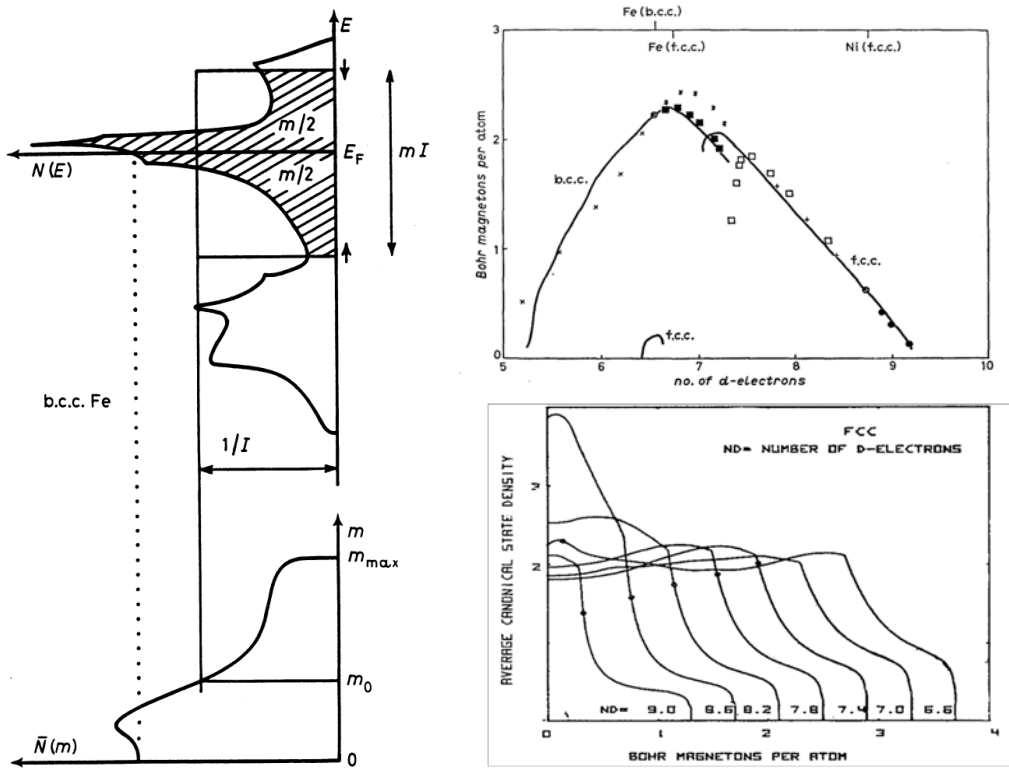


Fig. 13: Left: Stoner construction for ferromagnetism using the canonical, bcc d -DOS in Fig. 5 for Fe. Dotted/full line: $I = 0/65$ mRy (from Ref. [12]). Right bottom: Canonical fcc $\bar{N}(n_d, m)$ for varying n_d as functions of m . The dots are at the crossing with $1/I$ at normal pressure. The reason why m_{\max} is not exactly $10 - n_d$ is that the d -projected DOS for fcc Pd, rather than the fcc canonical d -band in Fig. 5 was used [30]. Right top: Slater-Pauling curve showing the magnetization, m , as a function of d -band occupation, n_d . The full curves were calculated with the procedure shown to the left and below using the experimental structures (hcp taken as fcc) and with I and n_d interpolated between the values calculated for Fe, Co, and Ni. Experimental values were obtained for the pure metals and intermetallic alloys (\bullet NiCu, $+$ CoNi, \cdot FeCo, \square NiFe fcc, \blacksquare NiFe (bcc), \times FeCr). From Ref. [30].

bit below the big bcc DOS peak, $\bar{N}_d(6.5, m)$ starts to increase from $N(\varepsilon_F)$ for m increasing, but as soon as $\varepsilon_{F\downarrow}$ has passed above the top of the peak, $\bar{N}(n, m)$ drops and eventually hits the plateau caused by the t_{2g} states at the top of the d -band (see Fig. 5). \bar{N} finally vanishes when all $m_{\max} \sim 3.5$ holes at the top of the d -band are filled. Knowledge about the interaction, I , and with $\mathcal{H}=0$, allows us to find the selfconsistent value of m as the solution of: $\bar{N}(n, m) = I^{-1}$. We see that $I \sim 67$ mRy does not suffice to split $\varepsilon_{F\downarrow}$ beyond the edge of the t_{2g} plateau and $\varepsilon_{F\uparrow}$ below the bottom of the pseudogap. So Fe is not, like fcc Ni and hcp Co, a strong ferromagnet, but has a moment of $m=2.2 \mu_B/\text{atom}$ with 54% e_g character [8], as may be imagined from Fig. 5 and which is in good agreement with the experimental 53%. Similarly, for fcc Ni the Stoner condition with $I=73$ mRy and $n_d=8.7$ yields a moment of $0.68 \mu_B/\text{atom}$ with only 24% e_g -character, also in agreement with the experimental 19% [45]. The canonical fcc $\bar{N}(8.5, m)$ shown in Fig. 13 at the bottom to the right (turned by 90° with respect to the bcc $\bar{N}(6.5, m)$ to

the left) is approximately the one appropriate for Ni, and the dot marks the crossing with I^{-1} . In the right-hand, upper part of Fig. 13, we show in full line the ferromagnetic moments, m , as functions of n_d , calculated as shown on the left-hand side using the experimental structures (hcp taken as fcc) and with I and n_d interpolated between the values calculated for Fe, Co, and Ni. This so-called Slater-Pauling curve is compared with experimental values (dots) for the pure metals and intermetallic alloys. So-called strong ferromagnets are those with $\varepsilon_{F\downarrow}$ split above the top of the d -band and thus have $m = 10 - n_d$. The late fcc and hcp metals have high I -values (Fig. 10), and the high peak in the d -DOS at $n_d=8.5$ (Fig. 5) keeps the average DOS, $\bar{N}(n_d, m)$, above I^{-1} for all $m \lesssim 10 - n_d$ and for n_d decreasing from 10 to about 7.2 (Fig. 13 bottom right). At that point, I^{-1} gets above $\bar{N}(n_d, m)$ for all m . This drop of m happens also for the real alloys, but at a slightly larger n_d . For n_d decreasing below 7.3, the structure changes from fcc (hcp) to bcc and the Fermi level enters the large peak in the bcc DOS and thereby makes $\bar{N}(n_d, m)$ reach above I^{-1} . By $n_d=6.5$, we have the situation of bcc Fe illustrated to the left in the figure. For n_d decreasing further, I^{-1} increases and ε_F moves down-hill on the low-energy side of the large peak, whereby $\bar{N}(n_d, m)$ flattens out, and by $n_d \sim 5.2$, it is entirely below I^{-1} .

With pressure, mainly the band-width parameter Δ_d in the Hamiltonian (8) changes; increasing approximately like s^{-5} (note the difference between Δ_d and the exchange splitting Δ). This means that if $\bar{N}(n, m)$ refers to the canonical S - or S^γ -scale, the self-consistency condition becomes: $\bar{N}(n, m) = \Delta_d(s)/I$, whereby the \bar{N} vs. m curves at the bottom of Fig. 13 become pressure vs. m curves (see Fig. 5 in Ref. [30]). Under pressure, bcc Fe thus loses its moment gradually. Had we constructed $\bar{N}(6.5, m)$ using the hcp and fcc DOS curves shown in Fig. 5, \bar{N} would with m increasing from 0, start off from a somewhat lower value than for bcc Fe, but then stay constant, because the canonical DOS for the hcp and fcc structures are fairly flat around $n_d=6.5$, until dropping to zero near 3.5. For fcc and $n_d=6.6$, this is shown in the bottom right-hand part of Fig. 13. This means that, since for hcp and fcc Fe $\bar{N}(n, 0)$ is slightly larger than Δ_d/I at normal pressure, this changes as Δ_d is increased by a slight lattice compression, and the moment vanishes abruptly (hcp) or within a small pressure range (fcc) (Figs. 4-6 in Ref. [30]).

Had it not been for its ferromagnetism, Fe would not have been bcc, but hcp like Ru and Os with $n_d \sim 6.5$. This is clearly seen in Fig. 12 on the right-hand side and at the bottom to the left. The top-left ‘‘bond-energy’’ curve can be used for each direction of spin in bcc Fe to realize that its bond energy, the value at $n_d = 6.5$ of the chord connecting the values at $6.5 \mp m$, is *lower* (the sum of one-electron kinetic energies is higher) than those of hcp and fcc paramagnetic Fe. The energy gain comes from the exchange energy, $-m^2 I/4$. Compression reduces m as explained above, and the point where gain of exchange energy equals the cost in kinetic energy gives the critical value of the moment for which the structural phase transition occurs. The observed phase transition from bcc ferromagnetic to hcp non-magnetic Fe, occurs at a pressure of 100 kbar when m and s have both been reduced by a few per cent. (Actually, the stability of ferromagnetic bcc Fe over non-magnetic hcp Fe is marginal and depends on the DFT used [46]).

The loss of kinetic energy associated with magnetism may in Stoner theory be described as contribution to the pressure given by:

$$3\mathcal{P}_{d\text{magn}}\mathcal{V} = -\frac{\delta \ln \Delta_d}{\delta \ln s} \int_0^m \frac{m' dm'}{2\bar{N}(n, m)} - \frac{1}{\mu_d} (m^2 I + 2\mu_B \mathcal{H}). \quad (19)$$

Here, $-\delta \ln \Delta_d / \delta \ln s \sim 5$ and $\mu_d^{-1} = s^2 \Delta_d$ was shown in Fig. 9. From Fig. 8, we realize that the magnetic metals do have relatively large WS radii (open dots), but that LSD calculations (open triangles) for Fe, Co, and Ni only account for a fraction of these anomalies.

Turning now to fcc Ni under pressure, we need the canonical fcc $\bar{N}(8.7, m)$ -curve, but shall use $\bar{N}(8.5, m)$ which is shown at the bottom right-hand side of Fig. 13 as a proxy. We see that the dot marking its crossing with Δ_d/I at zero pressure, can be raised by the large factor ~ 2.4 , before reaching the peak at $m \sim 0$, which is the one in the canonical DOS caused by the saddle-points P_1 and P_2 in the 5th band (Fig. 5). 2.4 is the factor by which the d -bandwidth ($\propto \Delta_d$) can be increased before an fcc ferromagnet (FM) with 8.5 d -electrons loses its moment. Since Ni under pressure keeps its fcc structure, it also keeps its moment up to several Mbars because $d \ln \Delta_d / d \ln s \sim -5$, $\mathcal{B} \sim 2$ Mbar, and $\partial \mathcal{B} / \partial \mathcal{P} \sim 4$ [29].

If we now increase the saturation moment from the $0.6 \mu_B$ of Ni ($0.8 \mu_B$ for the proxy) by decreasing the number of d -electrons, i.e. moving up the Slater-Pauling curve in Fig. 13 and the Fermi level moving down the low-energy side of the canonical fcc DOS peak and into the u-shaped valley in Fig. 5, the fcc $\bar{N}(n_d, m)$ -curves lose their peak and become flat once the valley is entered. This happens when $n_d \sim 8$. From the values of $\bar{N}(n_d, 0)$, we see that the bottom of the valley is reached when $n_d \sim 7.4$, and that by ~ 6.6 the Fermi level has moved up so high on the low-energy side of the valley that the DOS exceeds Δ_d/I and a FM with a low moment becomes stable. The large-moment FMs exist as long as the high DOS peak at $n_d = 8.6$ continues to raise the average $\bar{N}(n_d, m)$ above Δ_d/I , which happens until n_d falls below 7.3. The $8 \gtrsim n_d \gtrsim 6.5$ region is that of the Invar alloys which keep their atomic volume constant over a useful range of temperatures. In the early 60ies, this was explained as the effect of competing large-moment large-volume and low-moment low-volume states [47]. With pressure, the Δ_d/I -dots move up their respective fcc $\bar{N}(n_d, m)$ -curves in Fig. 13. We see that the initial slope, $-dm/d\mathcal{P}$, stays constant until $n_d=7.4$, but that the pressure where the moment disappears in a 1st-order transition, corresponding to the Δ_d/I -line touching the maximum of $\bar{N}(n_d, m)$, falls rapidly as we move away from Ni.

On exhibit at the entrance to the mineralogical museum in Copenhagen is a 20 tons iron-nickel meteorite found at Cape York in Greenland. It consists of a bcc and an fcc phase with a common orientation throughout the entire meteorite, which therefore seems to have been a single crystal in the mother asteroid. The fcc phase (taenite) has been found to be a simple, ordered FeNi alloy consisting of alternating (100) layers of Fe and Ni, which disorders by heating to 750 K for 50 hours [48]. This demonstrates that the meteorite has not –since its formation in the parent planet– been reheated to a temperature above 730 K for longer than 50 hours.

Attempting to get “insight” to the properties of the Earth’s inner core, we [49] performed a proper LSD calculation for taenite resulting in Fig 14. In the ferromagnetic DOS, we see the \uparrow

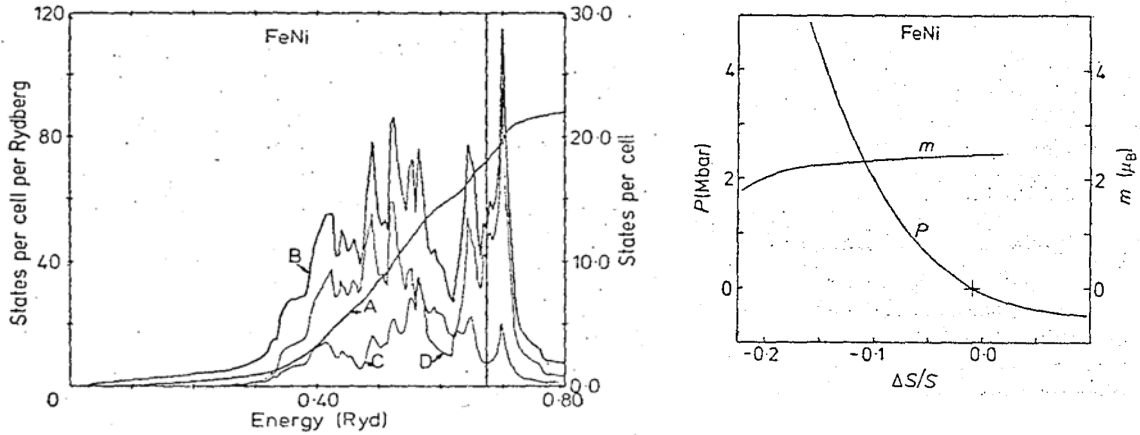


Fig. 14: Results of LSD LMTO calculation for fcc FeNi (taenite). Left: Number(A)- and density(B) of states per FeNi. Fe(C)- and Ni(D)-projected DOS. Right: FM magnetization and Pressure as functions of the relative deviation of the WS radius from its experimental value at 1 kbar. From Ref. [49].

and \downarrow fcc peaks, split on either side of ε_F , and we also see that the Fe(C)- and Ni(D)-projected DOS share these peaks, but with the dominant weight on Fe, because C_d lies higher- and Δ_d is broader in Fe than in Ni. Most remarkable: The FM magnetization stays robustly above $2 \mu_B$ for pressures up to 5 Mbar (causing a 15% compression of s). Using, instead, the rigid-band picture and \bar{N} (7.7, m) in Fig. 13, m would drop significantly already at a 20% reduction of Δ_d/I , i.e. at a mere 4% reduction of s . So apparently, taenite is special. We were fascinated by the thought that the earth's core could be a ferromagnet, but 40 years ago we did not know how to treat fluctuations at high temperatures.

For more recent LSD calculations of the spin and *orbital* moments in Fe, Co, and Ni, see Ref. [50].

3.3.2 Spin spirals

One may go beyond collinear spin-polarization by allowing the direction of spin-quantization to depend on \mathbf{r} , or simpler and more relevant for magnetic order, on the site, \mathbf{t} . Let us consider the case where all spin-quantization axes lie in the same plane, i.e., not on a cone. Provided that spin-orbit coupling (causing magnetic anisotropy) is neglected, it does not matter which plane we take. We choose the xy -plane and let $\phi(\mathbf{t})$ give the direction of spin on site \mathbf{t} . With the matrix for hopping from site \mathbf{t} and spin σ to site \mathbf{t}' and spin σ' being $h_{\mathbf{t}\mathbf{t}'}\delta_{\sigma\sigma'}$ in the *global* spin frame, it becomes:

$$\tilde{h}_{\mathbf{t}\sigma,\mathbf{t}'\sigma'} = \left\{ \begin{array}{cc} \uparrow & \cos \frac{\phi(\mathbf{t}')-\phi(\mathbf{t})}{2} & i \sin \frac{\phi(\mathbf{t}')-\phi(\mathbf{t})}{2} \\ \downarrow & i \sin \frac{\phi(\mathbf{t}')-\phi(\mathbf{t})}{2} & \cos \frac{\phi(\mathbf{t}')-\phi(\mathbf{t})}{2} \end{array} \right\} h_{\mathbf{t}\mathbf{t}'}$$

in the *local* frame. Here, $h_{\mathbf{t}\mathbf{t}'}$ could be the ASA Hamiltonian (6), $H_{\mathbf{t}'\mathbf{t}m',\mathbf{t}lm}^\gamma$, before Fourier-summing it to \mathbf{k} -space. Including the exchange splitting, $\Delta(\mathbf{t})$, the total one-electron Hamilto-

nian in the *local* frame is therefore

$$\tilde{H}_{\mathbf{t}\sigma,\mathbf{t}'\sigma'} = \begin{array}{cc} & \uparrow \\ \uparrow & -\frac{\Delta(\mathbf{t})}{2}\delta_{\mathbf{t},\mathbf{t}'} + \cos\frac{\phi(\mathbf{t}')-\phi(\mathbf{t})}{2}h_{\mathbf{t}\mathbf{t}'} & i\sin\frac{\phi(\mathbf{t}')-\phi(\mathbf{t})}{2}h_{\mathbf{t}\mathbf{t}'} \\ \downarrow & i\sin\frac{\phi(\mathbf{t}')-\phi(\mathbf{t})}{2}h_{\mathbf{t}\mathbf{t}'} & \frac{\Delta(\mathbf{t})}{2}\delta_{\mathbf{t},\mathbf{t}'} + \cos\frac{\phi(\mathbf{t}')-\phi(\mathbf{t})}{2}h_{\mathbf{t}\mathbf{t}'} \end{array},$$

h_{00} is the on-site orbital Hamiltonian. $\Delta(\mathbf{t})$ is an orbital matrix, which is approximately diagonal, with Δ in the d -block, possibly with different e_g and t_{2g} elements, and zero in the sp -blocks. With Δ positive, \uparrow will be the majority spin.

If the sites, \mathbf{t} , now form a lattice and all atoms are equivalent, i.e. we have 1 atom per translational cell, then $h_{\mathbf{t}\mathbf{t}'} = h(\mathbf{t}' - \mathbf{t})$. If also $\Delta(\mathbf{t})$ and $\phi(\mathbf{t}') - \phi(\mathbf{t})$ are translationally invariant, i.e. equal to respectively Δ and $\phi(\mathbf{t}' - \mathbf{t})$, then the Hamiltonian, $\tilde{H}_{\mathbf{t}\sigma,\mathbf{t}'\sigma'} = \tilde{H}(\mathbf{t}' - \mathbf{t})_{\sigma,\sigma'}$, is translationally invariant and therefore diagonal in the Bloch representation

$$\tilde{H}(\mathbf{k})_{\sigma,\sigma'} = \begin{array}{cc} & \uparrow \\ \uparrow & -\frac{\Delta}{2} + \sum_{\mathbf{t}} e^{i\mathbf{k}\cdot\mathbf{t}} \cos\frac{\phi(\mathbf{t})}{2}h(\mathbf{t}) & i\sum_{\mathbf{t}} e^{i\mathbf{k}\cdot\mathbf{t}} \sin\frac{\phi(\mathbf{t})}{2}h(\mathbf{t}) \\ \downarrow & i\sum_{\mathbf{t}} e^{i\mathbf{k}\cdot\mathbf{t}} \sin\frac{\phi(\mathbf{t})}{2}h(\mathbf{t}) & \frac{\Delta}{2} + \sum_{\mathbf{t}} e^{i\mathbf{k}\cdot\mathbf{t}} \cos\frac{\phi(\mathbf{t})}{2}h(\mathbf{t}) \end{array}.$$

The hopping matrix, $h(\mathbf{t})$ becomes $h(\mathbf{k})$, e.g. $H_{l'm',lm}^\gamma(\mathbf{k})$, in the Bloch representation. For a *spin spiral* of wave-vector \mathbf{q} ,

$$\phi(\mathbf{t}) \equiv \mathbf{q} \cdot \mathbf{t}, \quad (20)$$

we therefore get

$$2\tilde{H}(\mathbf{q},\mathbf{k})_{\sigma,\sigma'} = \begin{array}{cc} & \uparrow \\ \uparrow & -\Delta + h(\mathbf{k} + \mathbf{q}) + h(\mathbf{k}) & h(\mathbf{k} + \mathbf{q}) - h(\mathbf{k}) \\ \downarrow & h(\mathbf{k} + \mathbf{q}) - h(\mathbf{k}) & \Delta + h(\mathbf{k} + \mathbf{q}) + h(\mathbf{k}) \end{array}$$

where we have redefined \mathbf{k} to have its origin at $-\mathbf{q}/2$. This representation in which the local exchange splitting, Δ , appears in the diagonal and the hopping difference in the off-diagonal, is the natural one when Δ is large and \mathbf{q} is small. However, a unitary transformation brings the Hamiltonian into the simplest form

$$\tilde{H}(\mathbf{q},\mathbf{k}) = \begin{array}{cc} & (\uparrow - \downarrow)/\sqrt{2} & (\uparrow + \downarrow)/\sqrt{2} \\ (\uparrow - \downarrow)/\sqrt{2} & h(\mathbf{k}) & \frac{\Delta}{2} \\ (\uparrow + \downarrow)/\sqrt{2} & \frac{\Delta}{2} & h(\mathbf{k} + \mathbf{q}) \end{array}, \quad (21)$$

where the paramagnetic bands are in the diagonal and Δ is in the off diagonal. For small Δ , this form is the natural one.

We recapitulate: All spins have been chosen to lie in the same plane, which in the absence of spin-orbit coupling is arbitrary. In all planes perpendicular to \mathbf{q} , all spins are identical, but as we progress by \mathbf{t} in the plane, they turn by the angle $\mathbf{t} \cdot \mathbf{q}$. For $\mathbf{q}=\mathbf{0}$, we get back to the FM Hamiltonian (but doubly degenerate). If in the xy -plane the lattice is square with lattice

constant 1, $\mathbf{q}=(\pi, 0)$ gives an antiferromagnet (AF) with stripe-order and $\mathbf{q}=(\pi, \pi)$ an AF with checkerboard-order.

Incommensurability is *no* complication as long as SO coupling is neglected. We simply must have the same Abelian group in configuration and spin space. In configuration space, the generators of this group are the primitive lattice translations. In spin space, they are the primitive lattice translations, times turning the axes of spin quantization by a fixed angle: Subject yourself (being either a charge or a spin) to such an operation, look around, and you cannot see that you moved. It is of course essential that only the direction, and not magnitude of the magnetization changes. The band structure in the presence of the spin spiral has lost the crystalline point-group symmetry, but the number of states remains 1 per primitive cell and BZ, i.e.: the problem can be solved for any \mathbf{q} without increasing the size of the primitive cell. This is all not obvious and I believe that Sadratskii was the first who realized it [51].

The reduction to the Stoner model has the conceptual advantage of cutting the self-consistency loop into a band-structure part, which for a given spin order, \mathbf{q} , site, and orbital-dependent exchange-splitting field, Δ , yields the site and orbital-dependent spin-moments, $m(\mathbf{q})$, plus a self-consistency condition which states that $m(\mathbf{q})/\Delta = I^{-1}$. The band-structure part gives insight into the complicated static response, $\chi(\mathbf{q}) \equiv m(\mathbf{q})/\Delta$, of the non-interacting system, and not only in the linear regime [52].

3.3.3 Local exchange couplings

The *spatial* dependence of the magnetic coupling in metals, i.e. the change in total energy upon turning the direction of one spin with respect that of a neighbor is needed to calculate for instance Curie temperatures and magnon spectra. By considering infinitesimal spin rotations rather than spin flips, Lichtenstein and Katsnelson could use the force theorem locally and derived an elegant expression for the second derivative of the total energy in terms of the one-electron Green function, $[(\varepsilon - i0) \delta_{RR'} \delta_{ll'} \delta_{mm'} - H_{Rlm, R'l'm'}^\gamma]^{-1}$. Their expression has become a standard tool for complex magnetic systems and made it possible to simulate magnetic properties of real materials via *ab initio* spin models [53–55].

3.4 Fermi surfaces and mass renormalizations

For the elemental metals in the *4d*- and *5d*-series the Fermi surfaces (FSs) calculated using LDA (or Mattheiss-Slater) agree with de-Haas-van-Alphen (dHvA) measurements of the extremal areas of the cyclotron orbits on the FS to an accuracy better than what corresponds to a 15 mRy-shift in the position of the *d*- with respect to the non-*d* bands [10]. For the fcc late *5d*- and *4d*-metals [15], the agreement is even beyond 5 mRy – and best for Pt and Pd where over 80% of the DOS at the Fermi level, $N(\varepsilon_F)$, is contributed by the large, 5th-band *d*-hole sheet shown in Fig. 5, the same, which in combination with the larger Stoner *I* (Fig. 10) and the smaller 3d-bandwidth is responsible for the FM in fcc Ni.

Pd is nearly ferromagnetic and its uniform, static spin-susceptibility (17) is enhanced by a Stoner factor ~ 10 , over the Pauli value, which is proportional to $N(\varepsilon_F)$ like the electronic-

specific heat coefficient. In the late 60ies it had been suggested [56] that such ferromagnetically correlated, paramagnetic (PM) spin fluctuations would be detrimental for the singlet Cooper pairs formed via the electron-phonon interaction and, hence, could be the reason why Pd does not become a superconductor at low temperature like e.g. its neighbor Ir. Moreover, the interaction of the conduction electrons with these spin fluctuations would lead to an enhancement of the electronic mass and specific-heat coefficient, initially estimated –using a spherical FS– to be a factor 4. Comparison of the measured specific-heat coefficients with $N(\varepsilon_F)$ for the above-mentioned calculated band structures gave mass enhancements of 1.37 for Ir, 1.44 for Rh, 1.63 for Pt, and 1.66 for Pd [15]. Experimental results for the cyclotron masses (energy-derivatives of the extremal areas on the FS) did not exist for Ir, and dHvA for Rh only gave masses for the smaller orbits. They exceed the calculated band masses by factors around 1.1, except for the largest orbit where the mass enhancement was 1.3. So, presumably, the mass-enhancement for the large, 5th-band sheet, which for Rh and Ir is Γ -centered and closed, is the 1.44 obtained from the specific heat. Also for Pd, no masses could be detected from orbits around the 5th-band sheet, but only from a smaller d -like sheet and the large sp -like sheet. In all those cases, the masses exceeded those calculated by factors 1.5-1.7, which is consistent with the factor 1.66 obtained from the specific heat. For Pt, masses from several orbits on all three sheets could be measured and were found to be enhanced by factors of 1.44, 1.45, and 1.54 for the orbits on the sp -sheet, and by 1.30, 1.68, and 1.72 for those on the large d -hole sheet; thus consistent with the specific heat enhancement. In the 80ies, this was supported by more detailed experiments and analyses [57]. In conclusion, a mass enhancement of ~ 1.4 was attributed to the electron-phonon interaction ($\lambda_{ep} \sim 0.4$) [58]. This agreed with McMillans estimate for the superconductor Ir and with rigid-MT calculations of λ_{ep} in the early 80ies, and with S.Y. and D.Y. Savrasov's DFT linear-response calculations [59] in the mid 90ies. The remaining mass-enhancement in Pd was attributed to the PM spin fluctuations ($\lambda_{e-sf} \sim 0.25$). The results of the first spin-fluctuation calculation using LDA bands to calculate e.g. $\chi(\mathbf{q}, \mathbf{q}', \omega)$ [60] and of Savrasov's linear-response calculations from the late 90ies [61] agreed with this small value.

For the exchange-split FS of ferromagnetic bcc Fe, dHvA experiments [62] found surprisingly good agreement with the FS calculated with LSD [63], e.g., the sum of- and difference between- the numbers, $n_{\uparrow}=5.08$ and $n_{\downarrow}=2.93$, extracted from the extremal areas agree closely with the number of electrons, 8, and Bohr magnetons, 2.12. The mass-enhancements, found to range between 1.5 and 3.0, were larger than for, e.g., Pd.

4 Post 1986

The discoveries beginning in 1986 of high-temperature superconducting materials (HTSCs) which without doping are AF insulators –as is the case for cuprates– or AF metals –in case of iron pnictides and chalcogenides– caused enormous interest in the role of AF-correlated spin fluctuations as mediators of the superconductivity [64–67].

In the ruthenates, depending on the distortion of the RuO_6 -octahedra building these corner-sharing perovskites [68, 69], not only AF- but also FM spin fluctuations exist. This was shown

by Mazin and Singh by demonstrating, first, that the diverse magnetic properties of the 3D ruthenates, SrRuO_3 , CaRuO_3 , and Sr_2YRuO_6 follow from the Stoner band-picture as consequences of differences in oxygen positions and Ru-O-Ru hopping paths (Ca makes the oxygen octahedra rotate and Y blocks the paths). In these materials the detailed lattice structure is thus crucial for the magnetic properties. Next, they found 2D Sr_2RuO_4 to have strong FM spin fluctuations causing susceptibility- and mass renormalizations, as well as a critical temperature for triplet p -wave-pairing superconductivity, which agreed quantitatively with observations. The subsequent experimental observation of AFM in Ca_2RuO_4 , lead Mazin and Singh to calculate the susceptibility of Sr_2RuO_4 for all \mathbf{q} -vectors. That revealed competing AF spin fluctuations (confirmed later by neutron scattering), and concomitant singlet d -wave pairing. This, finally, led them to suggest that the actual superconducting ground state of Sr_2RuO_4 is determined by a competition between the p - and d -wave-pairing states [70].

4.1 ARPES

The intensive interest in HTSC lead to a development of angle-resolved photo-electron spectroscopy (ARPES) which, by the end of the millennium, was able to observe single-particle excitations from the occupied bands with 2-meV accuracy and 0.2° angular resolution and thereby, in some people's view, obviated the need for band-structure calculations. But of course, ARPES has problems of its own, such as surface-, final-state, and matrix-element effects [71].

After much smoke had cleared, the LDA FSs predicted a decade earlier for the HTSCs in their normal state usually turned out to be correct, e.g. for the $\text{YBa}_2\text{Cu}_3\text{O}_7$ FS with sheets from the two plane-bands and the chain-band [72–74]. This being settled –more or less– the challenge was –and remains– to observe how the bands get from k_F , where they agree with the LDA, but have a smaller, renormalized slope to join the LDA bands again, deeper down, below the Fermi level. These are the effects of the real part of the self-energy describing the interactions with e.g. phonons and spin-fluctuations. The imaginary part produces broadening. The mass renormalization is a measure of the strength of the interaction, and the energy over which this ζ -shaped anomaly (kink) occurs, is determined by the energy-spectrum of the interacting boson. For phonons, this energy is the Debye energy, for spin-fluctuations it is wider, but less well known. And then, there are competing phases. To observe and understand what happens to the anomaly when entering the superconducting state is the holy grail, so let us therefore leave the HTSC and return to Pd.

For fcc Pd, it has been possible with polarization-dependent, high-resolution ARPES to study the self-energy effects of the sp -like band along ΓK , where the large d -sheet (Fig. 5) is avoided [75]. The anomaly was found to be 20 meV below ε_F , in agreement with the Debye energy, and the renormalization of the Fermi velocities were found to yield $\lambda_{ep}=0.39\pm 0.05$ in agreement with the above-mentioned, previous studies. For this sp -like band, it was estimated that $\lambda_{ee} \sim 0.02$. Analysis of the anomaly indicated a possible contribution from PM spin-fluctuations down to 100 ± 50 meV below ε_F , and that $\lambda_{e-sf} \sim 0.06$ for the sp -like band.

4.2 Static and dynamical mean-field approximations

LSD worked surprisingly well for the elemental metals. Even for the actinides and the transition-metal oxides, CaO through NiO, it reproduced the onset of antiferromagnetism and the associated large lattice expansion upon passing the middle of the series [34]. But LSD failed to reproduce the proper band gap, by an order of magnitude in MnO and NiO, and FeO and CoO were even metals! However, it was not until 5 years later when LSD was applied unwisely to the Mott insulator NiO [76], and another 4 years when it failed to reproduce the antiferromagnetism –a ground-state property– in undoped La_2CuO_4 – I being ~ 5 times too small– that the failures became widely recognized [77].

This then gave birth to the self-energy-corrected (SIC) LDA [78], a proper DFT which, however, gave bad bands, and the LDA+ U which, like LSD, helped the functional, but by using Hubbard U instead of Stoner I in a static mean-field approximation [79, 80]. Values of U , the properly screened, on-site Coulomb integral, had previously been calculated by constrained LDA [81, 82] for use in the Anderson impurity model whose Coulomb repulsion is merely on the impurity site [83]. LDA+ U works successfully for insulators with spin- or orbital order [84–87], but the description of (finite-temperature) paramagnetic Mott-insulating states, or of spectra of correlated metals are entirely out of reach. This problem is related to the dynamical nature of electron correlations not accounted for in static mean-field approximations.

In 1989, Metzner and Vollhardt [88] had observed that the single-band Hubbard model with Coulomb repulsion, U , between two electrons on the same site and integral, t , for hopping between nearest-neighbor sites becomes far more tractable, while preserving much of its interesting correlation physics, if taken at infinite dimensions (after appropriate scaling). Moreover, the correlation energy in the weak-coupling limit turns out to be nearly the same for $D=\infty$, as for $D=3$. Hence, the $D=\infty$ -Hubbard model seemed to be not only simple, but also realistic.

(Although two decades earlier, I had set out to provide many-body theorists with a simple way to obtain realistic band structures and had exploited, that in metals there are usually far more neighbors than lobes in a d -orbital, had I come across Ref. [88], I could not have cared less. This is the danger of having no training in many-body physics).

Georges and Kotliar [89] soon realized that the $D=\infty$ -Hubbard model can be mapped exactly onto the Anderson impurity model –supplemented by a self-consistency condition for the energy-dependent (dynamical) coupling to the non-interacting medium. Hence, the quasiparticle peak of the Hubbard model may arise self-consistently from the Kondo resonance of the impurity model [90]. So what they achieved was to construct a mean-field picture of the Hubbard model which becomes exact as $D \rightarrow \infty$, and to provide an idea about how to solve the $D=\infty$ -Hubbard model. The immediate question was whether the $D=\infty$ -Hubbard model at half filling exhibits a metal-insulator Mott transition in the high-temperature, paramagnetic phase, i.e. whether, upon increasing U , the quasiparticle peak will develop into a gap by transfer of weight to the lower and upper Hubbard bands. The affirmative answer was found within months by Georges and Krauth who solved the Anderson impurity problem numerically and, independently, also by Rozenberg, Zang, and Kotliar. This dynamical mean-field approximation

(DMFT) is what eventually opened the door for theoretical treatment of correlated electrons in real materials [91,92].

(Although we had, for the impurity model, been computing realistic Coulomb integrals and hybridization-functions, and for alloys had been computing band structures using the coherent-potential approximation [93], we did not get the idea to combine them).

By suggesting the so-called LDA++ scheme, Lichtenstein and Katsnelson [94] proposed how model Hamiltonians of strongly correlated materials could be derived from DFT and thereafter solved by techniques like the Hubbard-I approximation or DMFT [95]. Together with an independent, simultaneous contribution by Anisimov, Kotliar *et al.* [96], this work marks the birth of the LDA+DMFT scheme which brings numerical LDA realism to DMFT [97].

But since that is at the heart of this series of autumn schools, I will proceed with a short description of a few of the applications in which I happened to be involved.

4.3 Transition-metal oxides (TMOs)

The TM sp -orbitals are far more extended than its d -orbitals, and in the oxides, the former therefore hybridize stronger with the O $2p$ orbitals than the latter. This pushes the TM sp -bands up, above the top of the d -bands, and can formally be neglected. For most transition-metal oxides, the d -bands lie completely above the O $2p$ bands (see Fig. 2), and the hybridization between them splits the d -bands into e.g. t_{2g} - and e_g -subbands [69,98].

4.3.1 Wannier Orbitals

Since it makes the chemistry and physics intelligible, and because DMFT requires a small basis set of correlated single-particle orbitals [100], it has become customary to project out of the Rydbergs-wide DFT Band structure a set (or sets) of so-called maximally localized Wannier functions, which span for instance the O $2p$ and the TM d -bands, and, hence, have the TM sp -orbitals folded down into the tails of mainly the O $2p$ orbitals, or merely the e_g -band with the tails of the O $2p$ - as well as those of the sp - and t_{2g} -orbitals on the TM neighbors folded in.

We prefer to generate such Wannier orbitals (WOs) *directly*, as symmetrically orthonormalized, minimal basis sets of NMTOs [18]. These are like linear MTOs (LMTOs), which use a linear $\{\varphi(r), \dot{\varphi}(r)\}$ -expansion of the energy dependence of the partial waves. If the downfolding is massive and the range of the MTOs therefore long and their energy dependence strong, the expansion needs to be of higher than linear order, hence of order $N > 1$.

The WO's can also be used to form intelligible tight-binding (TB) models [98, 101]. For the HTSCs, we [102] for instance found the empirical trend (Fig. 4 in Refs. [103] or [104]) that the transition temperature, $T_{c \text{ max}}$, for optimal doping increases with the ratio t'/t between the 2nd and 1st-nearest-neighbor hopping integrals in a massively downfolded, half-full one-band model (Cu d^{9-x}). The connection between t'/t and the chemistry, i.e. the structures and compositions of the 15 different families of HTSCs whose t'/t are shown in the figure, we have understood: These hopping integrals are between effective Cu $3d_{x^2-y^2}$ orbitals sitting on a

square lattice with primitive translations $(1, 0)$ and $(0, 1)$, and with each Cu connected by oxygens at $(\frac{1}{2}, 0)$ and $(0, \frac{1}{2})$. The t -hop is along x , from $d_{x^2-y^2}$ at $(0, 0)$ to $d_{x^2-y^2}$ at $(1, 0)$, via O p_x at $(\frac{1}{2}, 0)$, or equivalently, along y . The t' -hop is from $(0, 0)$ to $(1, 1)$. In this description, all orbitals (partial waves) are thus folded down into one, effective Cu $d_{x^2-y^2}$ orbital. But this orbital does, of course, have tails of O $2p_x$ at $(\pm\frac{1}{2}, 0)$ and of O $2p_y$ at $(0, \pm\frac{1}{2})$, to which the hopping in an up-folded three-band model is antibonding $pd\sigma$. The t' hop is “around the corner” on the square CuO_2 lattice, and proceeds via a so-called axial orbital which is a particular hybrid of Cu $3d_{3z^2-1}$, Cu $4s$, apical O $2p_z$, and whatever the latter bonds covalently to, such as La $5d_{3z^2-1}$. Note that the TB Hamiltonian is now up-folded to have four orbitals. Apical oxygens are those forming the apexes of the elongated CuO_6 octahedron, and the t'/t trend is caused by differences in this elongation, i.e. distance to apical oxygen, and in what the $2p_z$ -orbital on the latter binds to out there in the “doping” layers. But the physics, the correlation with $T_{c \text{ max}}$, remains to be understood or disproved.

In the cuprates the center of the Cu $3d$ band is only a few eV above that of the O $2p$ bands and the hopping between the two is so large that they form a common band. The strongest hopping integral is $pd\sigma$ and it creates for the CuO_2 plane a bonding-, a non-bonding-, and an antibonding-band spanning about 8 eV in the LDA. It is the latter band which the above-mentioned t, t', t'' model describes.

4.3.2 Metal-insulator transition in V_2O_3

The theoretical Mott-transition is the one in the single-band Hubbard model investigated by Georges and Krauth, and by Rozenberg, Zang, and Kotliar. But the DMFT+LDA NMTO calculations in which I have been involved, of experimentally observed metal-insulator transitions in TMOs, all dealt with multi-band systems where the isostructural (not-symmetry breaking) metal-insulator transition was basically the opening a gap between occupied and unoccupied bands by moving them apart.

V_2O_3 , for instance, undergoes an isostructural phase transition from a paramagnetic metal (PM) to a paramagnetic insulator (PI) upon raising the temperature from 20°C to about 400° , the transition temperature depending on the Cr-content in the 1% range. All V atoms and all O atoms are equivalent, and since each V brings in 5 electrons and each O has two holes to be filled, there remains 2 electrons per V. The VO_6 octahedra are nearly perfect and since the $pd\sigma$ interaction is stronger than the $pd\pi$ interaction, the more antibonding V $3d$ -like e_g level lies above the less antibonding V $3d$ -like t_{2g} level. As a consequence, the electronic configuration is $\text{V } t_{2g}^2$. All three orbitals hop to their neighbors, and with 4 formula units per primitive cell in this corundum structure, the LDA band structure is a solid mess of 12 bands, spread over 2.5 eV and $1/3$ filled; a metal (see Fig. 15).

There is a slight displacement of the V ions along the 3-fold $[111]$ axis, away from the centers of their octahedra, so that the distance between a vertical ($\equiv 111$) V_2 -pair whose octahedra in this corundum structure share a (111) face, is slightly longer than the distance between the centers of their octahedra. The xy, yz , and xz orbitals therefore rehybridize into one orbital,

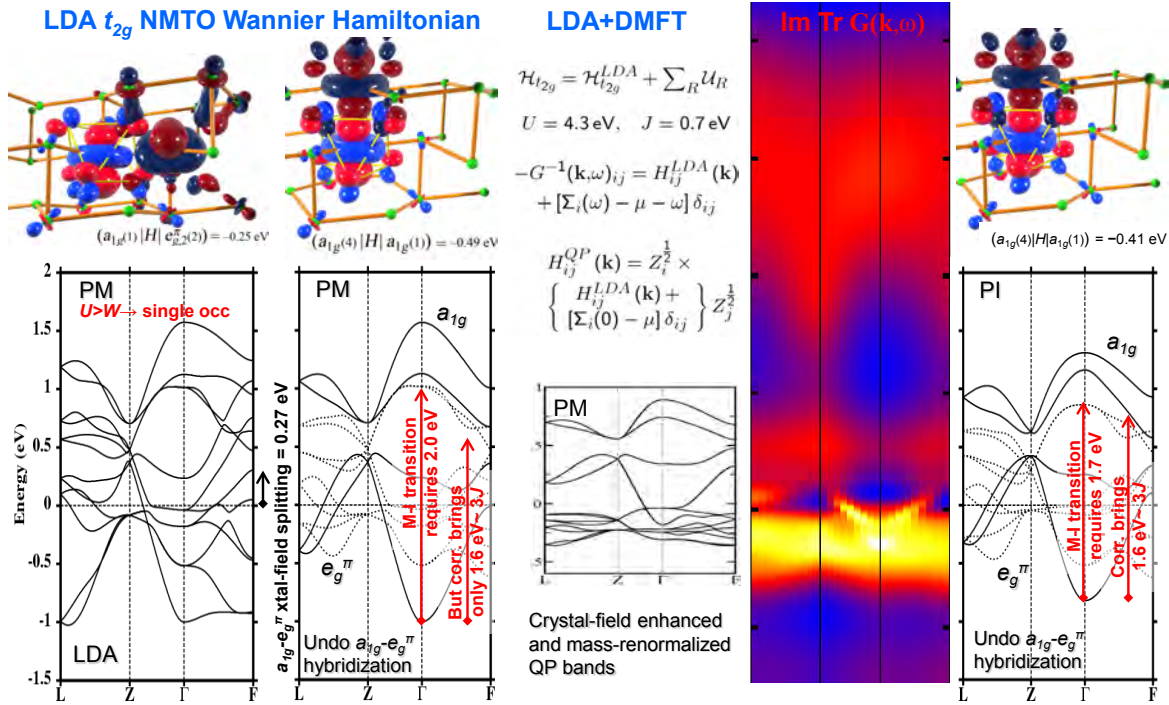


Fig. 15: The V_2O_3 story (see text). Three first panels: Experimental PM structure at 20° C. 1st panel: LDA hopping integral between effective a_{1g} (light) and e_g^π (dark) orbitals, -0.25 eV (upper left), and between a_{1g} orbitals on the vertical pair, -0.49 eV (upper right). LDA t_{2g} bands with- (lower left) and without (lower right) all a_{1g} - e_g^π hops. 2nd panel: Input Hamiltonian, DMFT output Hamiltonian, energy-linearized quasiparticle (QP) Hamiltonian and its band structure. 3rd panel: DMFT spectrum. 4th panel: Experimental PI structure at 400° C. LDA hopping integral between vertical pair, -0.41 eV (upper). LDA a_{1g} - e_g^π unhybridized band structure (lower). From Ref. [99].

$(xy + yz + xz) / \sqrt{3} = 3z_{111}^2 - 1$, of symmetry a_{1g} and two degenerate orbitals of symmetry e_g , called e_g^π , whereby the t_{2g} level is split into an upper a_{1g} and a lower, doubly degenerate e_g^π level. But this trigonal crystal-field splitting is 0.3 eV, an order of magnitude smaller than the bandwidth. At the Γ point, the center of the Brillouin zone, where a_{1g} and e_g^π cannot mix, the 4 a_{1g} levels are raised with respect to the 8 e_g levels by the 0.3 eV. The pure a_{1g} - and e_g^π - band structures, obtained by setting all hopping integrals between a_{1g} and e_g orbitals to zero, shows that the bottom of the a_{1g} and the top of the e_g band are at Γ , so that their distance, 2.0 eV of which the trigonal splitting contributes -0.3 and the hoppings 2.3 eV, can be read off the fully hybridized LDA bands.

The on-site Coulomb repulsion, however, prefers by $3J = 2.1$ eV to have one \uparrow electron in each e_g orbital, and none in the a_{1g} orbital. And this is basically what our DMFT calculation [99] at 100° C provides: It, first of all, “spin-polarizes” the bands and moves the \downarrow -weight to a very broad, incoherent upper Hubbard band lying $U = 4.2$ eV above the partly occupied \uparrow -band. For the latter, it then enhances the crystal-field splitting from 0.3 to 1.85 eV, whereby the a_{1g} bands essentially empties into the e_g^π band; the bottom of the former merely dips a 0.15 eV below the top of the latter.

With the splitting almost as large as the bandwidth, the a_{1g} - e_g hopping is strongly reduced, whereby the dispersion resembles that of pure LDA a_{1g} and e_g bands. But on top of this, there are quasiparticle renormalization by factors 2.5 and 5 for respectively the a_{1g} - e_g^π -bands, and, finally, inside the e_g^π -band there is strong e - e scattering which makes it incoherent. The metallic quasiparticles are those on the small a_{1g} sheet of FS.

Upon increasing the temperature across the metal-insulator transition, there is an increase of the so-called umbrella distortion which changes the LDA band structure. In particular, the distortion makes the effective $dd\sigma$ hopping integral between vertical V_2 pair decrease from -0.49 to -0.41 eV, whereby the distance between bottom of the a_{1g} and the top of the e_g^π LDA bands, is reduced from 2.0 to 1.7 eV. A Coulomb-enhanced crystal-field splitting of 1.85 eV would thus suffice to separate the bands. Sure enough, the DMFT calculation with the new LDA bands for the high-temperature structure, but the values of U and J unchanged, yields a small, insulating gap. This, we felt, demystified what for more than 30 years was considered *the* Mott transition.

4.4 Elemental metals

The e - e interaction effects in V_2O_3 are really drastic in comparison with those in Pd. Savrasov *et al.* [105] recently returned to the problem of calculating the effects on the self-energy, $\Sigma(\omega, \mathbf{k})$, from the interaction with the paramagnons in Pd and included the \mathbf{k} -dependence by combining the LDA with the fluctuational exchange (FLEX) approximation. By including ladder diagrams, FLEX can describe spin-fluctuations, in contrast to quasi-particle self-consistent GW (QSGW) approach (see below). As the results turned out to have only a small \mathbf{k} -dependence, they were compared with those of LDA+DMFT, and found to be in better agreement with experiments, yielding $\lambda=0.1-0.3$ for $U=1-2$ eV.

From ARPES for ferromagnetic bcc Fe, it was concluded in 2010 [106] that previous estimates of the d -band narrowing due to many-electron effects were too large due to neglect of SO-splitting in the LSD calculations, and of final-state transitions plus final-state broadening in the photoemission analysis. As a result, many-electron effects seem to narrow the d -band by merely 10%. In accord with the measured cyclotron masses [62] and the LSD calculations, the renormalizations of the Fermi velocities are in the range 1.5–3, presumably with $\lambda_{ep} \sim 0.4$ like for Pd, and a similar contribution from the electron-magnon interaction. However, whereas the two latter are expected to extend down to respectively 40 and 300 meV below ε_F , the self-energy anomaly was observed down to at least 500 meV, and finally attributed to many-electron effects.

The quasi-particle self-consistent GW (QSGW) approach which has been most successful in describing weak, but \mathbf{k} -dependent correlations, was recently applied to bcc Fe and fcc Ni by Schilfgaarde *et al.* [107]. For Fe, the agreement with the available FS data from dHvA was perfect, and the mass enhancements and the ARPES were well described. Due to its $\Sigma(\omega)$ lacking \mathbf{k} -dependence, DMFT does less well for ARPES. QSGW gave a 25% narrowing of the d -bandwidth, but that may have been due to neglect of SO splitting as suggested in Ref. [106].

For Ni, the PM part of the QSGW bands were in excellent agreement with experiments, but the exchange splitting was overestimated by a factor 2, even more than in the LSD, and the moment was overestimated by 20% and, hence, much worse than in the LSD. This problem is known for itinerant magnets, the iron pnictides, in particular. This failure was ascribed to the inability of GW to treat spin-fluctuations, and it was demonstrated by use of QSGW+DMFT, that a reasonable, simple cure is to add an external magnetic field adjusted get the moment right. The approach by Mazin *et al.*, who adjust the Stoner I , is at least based on Moriya's fluctuation theory [108].

Friedel once asked me about the real-space reason for the double-peak in the bcc DOS, which for instance is crucial for the martensitic transformation in steels. As seen in Fig. 5, the reason is *not* a separation of e_g - and t_{2g} -characters. But what *is* seen in this figure, is that in FM bcc Fe, the FS has mostly t_{2g} character (the \uparrow -sheet exclusively) and the big peak mostly e_g character. This was recently found to have consequences for the real-space exchange interactions [109]: The t_{2g} states are itinerant and determined by FS nesting, while the e_g states form localized moments which must be treated by DMFT. Most important was the subsequent insight [110] that for both fcc and bcc structures, and throughout the $3d$ series, the exchange coupling between an e_g orbital and a t_{2g} orbital on a near neighbor vanishes.

Most recently the *local* magnetic moments in Fe and Ni at ambient and Earth's-core conditions were studied [111] using an arsenal of methods, in particular DMFT. At normal pressure, the Curie temperature of Fe comes out about 30% too large while that of Ni is slightly too low. The authors (re-)discovered the van Hove singularities in fcc Ni and concluded that without these, Ni would not be a strong-coupling quantum magnet. Moreover: "The most important implication of our results for Ni comes from the observation that even at a pressure of hundreds of GPa (Mbars), the position and shape of these sharp features in the DOS do not change dramatically. Ni remains in its fcc structure up to even larger pressures and its magnetic moments, though smaller, are much more robust than those of Fe".

Well, in the process of substituting I with U , and static- with dynamical mean-field theory, insights from canonical band theory were apparently forgotten. In the end, AI may take over.

References

- [1] N. Bohr, *Zeitschrift für Physik* **9**, 1 (1922); spin and exclusion principle came later: W. Pauli, *Zeitschrift für Physik* **31**, 765 (1925)
- [2] L.D. Landau and E.M. Lifshitz: *Quantum Mechanics* (Pergamon, 1965)
- [3] M. Tinkham: *Group Theory and Quantum Mechanics* (McGraw-Hill, 1964) Ch. 6
- [4] W.A. Harrison: *Electronic structure and the properties of solids* (Dover, 1989)
- [5] R.M. Martin: *Electronic Structure: Basic Theory and Practical Methods* (Cambridge University Press, 2008)
- [6] C. Kittel: *Introduction to Solid State Physics* (Wiley, 1956)
- [7] K.H. Schwarz, *Chem. Phys.* **7**, 100 (1975)
- [8] O.K. Andersen and O. Jepsen, *Physica B+C* **91**, 317 (1977)
- [9] D.G. Pettifor, *J. Phys. F: Metal Phys.* **7**, 613 (1977);
ibid, **7**, 1009 (1977); *ibid* **8**, 219 (1978)
- [10] For a review, see: A.R. Mackintosh and O.K. Andersen:
The electronic structure of transition metals in Ref. [113]
- [11] H.L. Skriver: *The LMTO method: muffin-tin orbitals and electronic structure* (Springer, 1984)
- [12] O.K. Andersen, O. Jepsen, and D. Glötzel: *Canonical Description of the Band Structures of Metals* in Ref. [114] (where γ_i is named Q_i)
- [13] D.D. Koelling and B.N. Harmon, *J. Phys. C* **10**, 3107 (1977)
- [14] O.K. Andersen, *Phys. Rev. B* **12**, 3060 (1975)
- [15] O.K. Andersen and A.R. Mackintosh, *Solid State Commun.* **6**, 285 (1968);
O.K. Andersen, *Phys. Rev. B* **2**, 883 (1970)
- [16] R.M. Martin in Ref. [119]
- [17] P.E. Blöchl in Ref. [115]
- [18] O.K. Andersen: *NMTOs and their Wannier functions* in Ref. [116]
- [19] L Hodges, R.E. Watson, and H. Ehrenreich, *Phys. Rev. B* **5**, 3953 (1972)
- [20] O.K. Andersen, *Solid State Commun.* **13**, 133 (1973)
- [21] C.R. Brown, J.P. Kalejs, F.D. Manchester, J.M. Perz, *Phys. Rev. B* **6**, 4458 (1972)

- [22] O.K. Andersen and O. Jepsen, Phys. Rev. Lett. **53**, 2571 (1984)
- [23] R.O. Jones and O. Gunnarsson, Rev. Mod. Phys. **61**, 689 (1989), Sects. IVC, VI, and VII
- [24] E. Pavarini, p. 7.40 in Ref. [118]
- [25] O.K. Andersen, W. Klose, H. Nohl, Phys. Rev. B **17**, 1209 (1978)
- [26] U. von Barth and L. Hedin, J. Phys. C: Solid St. Physics **5**, 1629 (1972)
- [27] L.F. Mattheiss, Phys. Rev. **133**, A1399 (1964)
- [28] J.F. Janak, Phys. Rev. B **16**, 255 (1977); Janak's I is half- and his DOS twice our value
- [29] J. Madsen, O.K. Andersen, U.K. Poulsen, O. Jepsen in *Magnetism and Magnetic Materials 1975*, 327 (AIP, N.Y. 1976); U.K. Poulsen, J. Kollar, O.K. Andersen, J. Phys. F **6**, L241 (1976)
- [30] O.K. Andersen, J. Madsen, U.K. Poulsen, O. Jepsen, J. Kollar, Physica **86-88 B**, 249 (1977); J. Kollar *et al.* in *Proceedings of the VIII Symposium on Electronic Structure of Metals and Alloys* (Dresden, 1978)
- [31] V.L. Moruzzi, J.F. Janak, and A.R. Williams: *Calculated Electronic Properties of Metals* (New York, Pergamon 1978)
- [32] R. Car and M. Parrinello, Phys. Rev. Lett. **55**, 2471 (1985)
- [33] M.T. Yin, and M.L. Cohen, Phys. Rev. B **26**, 5668 (1982); M.L. Cohen in Ref. [114]
- [34] O.K. Andersen, H.L. Skriver, H. Nohl, B. Johansson, Pure and Appl. Chem. **52**, 93 (1979)
- [35] V. Heine, in H. Ehrenreich, F. Seitz, D. Turnbull (Eds.): *Solid State Physics* **35** (Academic Press, N.Y. 1980)
- [36] The force theorem considers an N -particle system whose Hamiltonian is the sum of the kinetic energy, two-body particle-particle interactions, and one-body interactions with an external potential. It gives expressions for the *internal* force on all particles in a region, Ω , which together with the force by the external potential on the particles in Ω keeps the system in a given stationary state, Φ . The derivation employs the variational principle with a trial function, $\Phi + d\Phi$ obtained from Φ by translating it rigidly from region Ω to $\Omega + d\mathbf{u}$, where $d\mathbf{u}$ is the direction of the force. The first result is that *the external force balances the kinetic force plus the two-body (e.g. electrostatic) force between the particles inside Ω and outside Ω* (the sum of the forces between the particles inside Ω cancel). Here, the kinetic force is the integral over the surface of Ω and the sum over all particles, j , of the kinetic stress tensor field, $\overleftrightarrow{\sigma}_j(\mathbf{r})$, which may be expressed in terms of the eigenvectors, $\psi_{jk}(\mathbf{r})$, and eigenvalues, n_{jk} , of the 1st-order density matrix. Transformation of the surface integral to a volume integral, transforms the kinetic force to the integral in Ω

of a kinetic force-density, $\mathbf{F}_{\text{kin}j}(\mathbf{r})$, expressed in terms of the occupation numbers, n_{jk} , and up to third derivatives of the natural orbitals, $\psi_{jk}(\mathbf{r})$. We then specialize to electrons and nuclei, and neglect the nuclear kinetic force, obtaining:

$$\mathbf{F}_{\text{kin}}(\mathbf{r}) = \frac{1}{2m} \sum_k n_k \left[\psi_k^*(\mathbf{r}) \left\{ \vec{\nabla} \nabla^2 \psi_k(\mathbf{r}) \right\} - \left\{ \nabla^2 \psi_k(\mathbf{r}) \right\}^* \left\{ \vec{\nabla} \psi_k(\mathbf{r}) \right\} \right].$$

If we *assume* that $\psi_k(\mathbf{r})$ satisfies a one-electron Schrödinger equation with a local, possibly state-dependent potential, $V_k(\mathbf{r})$, then $\mathbf{F}_{\text{kin}}(\mathbf{r}) = \sum_k n_k |\psi_k(\mathbf{r})|^2 \vec{\nabla} V_k(\mathbf{r})$, and we thus have the results that *the one-electron potential is that effective, external potential whose force balances the kinetic force, and the one electron energies are the eigenvalues of its Schrödinger equation*. But the exact result is the one for $\mathbf{F}_{\text{kin}}(\mathbf{r})$ given above. The LDA potential has μ_{xc} substituted by ϵ_{xc} on the surface of Ω , and this is what makes the homogeneous electron gas bind with $s_0 \sim 4.1$ a.u. [See also Ref. [5] and J. Gräfenstein and P. Ziesche, Phys. Rev. B **53**, 7143 (1996)].

- [37] D.G. Pettifor, Commun. Phys. **1**, 141 (1976) and Refs. therein
- [38] H.L. Skriver, Phys. Rev. B **31**, 1909 (1985)
- [39] N.W. Dalton and J. Hubbard, A.E.R.E. Harwell Rep. T.P. 327 (1968); Dalton and R.A. Deegan, J. Phys. C **2**, 2369 (1969); D.G. Pettifor, J. Phys. C **3**, 367 (1970)
- [40] J. Friedel in J.M. Ziman (Ed.): *The Physics of Metals* (Cambridge University Press 1969)
- [41] L.F. Mattheiss and D.R. Hamann, Phys. Rev. **33**, 823 (1986)
- [42] J.J. Duthie and D.G. Pettifor, Phys. Rev. Lett. **38**, 564 (1977)
- [43] S.H. Vosko and J.P. Perdew, Can. J. Phys. **53**, 1385 (1975); O. Gunnarsson and B.I. Lundqvist, Phys. Rev. B **13**, 4274 (1976); W. Kohn in Ref. [114]
- [44] O. Gunnarsson, J. Phys. F **6**, 587 (1976). Figs. 5 and 6 in particular
- [45] More accurate calculations giving for all 33 elemental metals values of the potential parameters, canonical bands, ground-state properties, and their pressure derivatives may be found in Ref. [12]
- [46] P. Bagno, O. Jepsen, O. Gunnarsson, Phys. Rev. B **40**, 1997 (1989)
- [47] L. Kaufman, E.V. Clougherty, R.J. Weiss, Acta Metall. **11**, 323 (1963)
- [48] J.F. Petersen, M. Aydin, J.M. Knudsen, Phys. Lett. **62** A, 192 (1977); F. Albertsen, J.M. Knudsen, G.B. Jensen, Nature **273**, 453 (1978)

- [49] H.L. Skriver and O.K. Andersen, Inst. Phys. Conf Ser. No. **39**, 100 (1978)
- [50] O. Eriksson, B. Johansson, R. C. Albers, A. M. Boring, M. S. S. Brooks, Phys. Rev. B **42**, 2707 (1990)
- [51] L.M. Sandratskii, Phys. Stat. Sol. (b) **135**, 167 (1986); J. Phys. Cond. Mat. **3**, 8565 (1991)
- [52] For an application to stripe order in FeAsLaO, see O.K. Andersen and L. Boeri, Ann. Phys. **523**, 8 (2011)
- [53] A.I. Lichtenstein in Ref. [117]
- [54] A.I. Lichtenstein, M.I. Katsnelson, V.A. Gubanov, J. Phys. F: Met. Phys. **14**, L125 (1984); Solid. State Commun. **54**, 327 (1985); A.I. Lichtenstein, M.I. Katsnelson, V.P. Antopov, V.A. Gubanov, J. Magn. Magn. Mater. **54-57**, 965 (1986); *ibid*, **67**, 65 (1987)
- [55] P. Bruno, Phys. Rev. Lett. **90**, 087205 (2003); M.I. Katsnelson and A.I. Lichtenstein, J. Phys.: Condens. Matter **16**, 7439 (2004)
- [56] N.F. Berk and J.R. Schrieffer, Phys. Rev. Lett. **17**, 433 (1966); *ibid* **19**, 644 (1967)
- [57] W. Joss, L.N. Hall, G.W. Crabtree, J.J. Vuillemin, Phys. Rev. B **30**, 5637 and 5646 (1984)
- [58] R. Heid in Ref. [119]
- [59] S.Y. Savrasov and D.Y. Savrasov, Phys. Rev. B **54**, 16487 (1996)
- [60] E. Stenzel and H. Winter, J. Phys. F: Metal Phys. **16**, 1789 (1986)
- [61] S.Y. Savrasov, Phys. Rev. Lett. **81**, 2570 (1998)
- [62] G.G. Lonzarich, J. Magn. and Magn. Mater. **45**, 43 (1984); *Fermi surface studies in ferromagnets* in Ref. [113]
- [63] J. Callaway and C.S. Wang, Phys. Rev. B **16**, 2095 (1977)
- [64] W. Pickett in Ref. [117]
- [65] B. Keimer in Ref. [117]
- [66] A. Tremblay in Ref. [117]
- [67] T. Maier in Ref. [120]
- [68] D. Singh in Ref. [116]
- [69] C. Franchini in Ref. [112]
- [70] I.I. Mazin and D.J. Singh, Phys. Rev. Lett. **82**, 4324 (1999) and Refs. therein

- [71] J. Minar in Ref. [92], *ibid* M. Sing
- [72] A. Damascelli, Z. Hussain, Z.X. Shen, Rev. Mod. Phys. **75**, 473 (2003)
- [73] O.K. Andersen, A.I. Liechtenstein, O. Jepsen, and F. Paulsen, J. Phys. Chem. Solids, Vol. **56**, 1573 (1995)
- [74] V.B. Zabolotnyy, S.V. Borisenko, *et al.*, Phys. Rev. B **76**, 064519 (2007)
- [75] H. Hayashi, K. Shimada, J. Jiang, H. Iwasawa, Y. Aiura, T. Oguchi, H. Namatame, M. Taniguchi, Phys. Rev. B **87**, 035140 (2013), Fig. 4, in particular
- [76] K. Terakura, T. Oguchi, A.R. Williams, J. Kübler, Phys. Rev. B **30**, 4734 (1984)
- [77] J. Zaanen, O. Jepsen, O. Gunnarsson, A.T. Paxton, O.K. Andersen, A. Svane, Physica C **153-158**, 1636 (1988)
- [78] A. Svane and O. Gunnarsson, Phys. Rev. Lett. **65**, 1148 (1990)
- [79] V. I. Anisimov, J. Zaanen, O.K. Andersen, Phys. Rev. B **44**, 943 (1991)
- [80] V. I. Anisimov, F. Aryasetiawan. A. I. Lichtenstein, J. Phys.: Condens. Matter **9**, 767 (1997)
- [81] O. Gunnarsson, O. K. Andersen, O. Jepsen, J. Zaanen, Phys. Rev. B **39**, 1708 (1989)
- [82] V.I. Anisimov, O. Gunnarsson, Phys. Rev. B **43**, 7570 (1991)
- [83] O. Gunnarsson in Ref. [116]
- [84] A. I. Lichtenstein, V. I. Anisimov, J. Zaanen, Phys. Rev. B **52**, R5467 (1995)
- [85] M. Cococcioni in Ref. [116]
- [86] E. Pavarini in Ref. [118]
- [87] E. Pavarini in Ref. [119]
- [88] W. Metzner and D. Vollhardt, Phys. Rev. Lett. **62**, 324 (1989)
- [89] A. Georges and G. Kotliar, Phys. Rev. B **45**, 6479 (1992)
- [90] M. Fabrizio in Ref. [119]
- [91] M. Kollar in Ref. [115]
- [92] E. Pavarini, E. Koch, D. Vollhardt, and A. Lichtenstein (eds.): *DMFT at 25: Infinite Dimensions*, Modeling and Simulation Vol. 4 (Forschungszentrum Jülich, 2014), [121]

- [93] J. Kudrnovsky, N.E. Christensen, O.K. Andersen, Phys. Rev. B **43**, 5924 (1991)
- [94] A.I. Lichtenstein and M.I. Katsnelson, Phys. Rev. B **57**, 6884 (1998)
- [95] F. Lechermann in Ref. [115]
- [96] V.I. Anisimov, A.I. Poteryaev, M.A. Korotin, A.O. Anokhin, G. Kotliar, J. Phys.: Condensed Matter **9**, 7359 (1997)
- [97] A.I. Lichtenstein in Ref. [92]
- [98] E. Pavarini in Ref. [116]
- [99] A.I. Poteryaev, J.M. Tomczak, S. Biermann, A. Georges, A. I. Lichtenstein, A. N. Rubtsov, T. Saha-Dasgupta, O.K. Andersen, Phys. Rev. B **76**, 085127 (2007)
- [100] J. Kunes in Ref. [115]
- [101] W.M.C. Foulkes in Ref. [118]
- [102] E. Pavarini, I. Dasgupta, T. Saha-Dasgupta, O. Jepsen, O.K. Andersen, Phys. Rev. Lett. **87**, 047003 (2001)
- [103] E. Pavarini in Ref. [117]
- [104] see E. Pavarini in Ref. [112]
- [105] S.Y. Savrasov, G. Resta, X. Wan, Phys. Rev. B **97**, 155128 (2018)
- [106] A.L. Walter, J.D. Riley, O. Rader, New J. Phys. **12**, 013007 (2010)
- [107] L. Sponza, P. Pisanti, A. Vishina, D. Pashov, C. Weber, M. van Schilfgaarde, S. Acharya, J. Vidal, G. Kotliar, Phys. Rev. B **95**, 041112 (2017)
- [108] L. Ortenzi, I.I. Mazin, P. Blaha, L. Boeri, Phys. Rev. B **86**, 064437 (2012)
- [109] Y.O. Kvashnin, R. Cardias, A. Szilva, I. Di Marco, M.I. Katsnelson, A.I. Lichtenstein, L. Nordström, A.B. Klautau, O. Eriksson, Phys. Rev. Lett. **116**, 217202 (2016)
- [110] R. Cardias, A. Szilva, A. Bergman, I. Di Marco, M.I. Katsnelson, A.I. Lichtenstein, L. Nordström, A.B. Klautau, O. Eriksson, Y.O. Kvashnin, Sci. Rep. **7**, 4058 (2017)
- [111] A. Hausoel, M. Karolak, E. Sasioglu, A. Lichtenstein, K. Held, A. Katanin, A. Toschi, G. Sangiovanni, Nat. Commun. **10**, 1038 (2017)
- [112] E. Pavarini, E. Koch, P. Coleman (Eds.): *Many-Body Physics: From Kondo to Hubbard*, Reihe Modeling and Simulation, Vol. 5 (Forschungszentrum Jülich, 2015), [121]
- [113] M. Springford (Ed.): *Electrons at the Fermi Surface* (Cambridge UP, 1980)

- [114] F. Bassani, F. Fumi and M.P. Tosi (eds.): *Highlights of Condensed-Matter Theory*, Course LXXXIX, International School of Physics “Enrico Fermi”, Varenna, Italy, (North-Holland, 1985)
- [115] E. Pavarini, E. Koch, D. Vollhardt, and A. Lichtenstein (Eds.):
The LDA+DMFT approach to correlated materials,
Reihe Modeling and Simulation, Vol. 1 (Forschungszentrum Jülich, 2011), [121]
- [116] E. Pavarini, E. Koch, F. Anders, and M. Jarrel (Eds.): *From Models to Materials*,
Reihe Modeling and Simulation, Vol. 2 (Forschungszentrum Jülich, 2012), [121]
- [117] E. Pavarini, E. Koch, U. Schollwöck (Eds.):
Emergent Phenomena in Correlated Matter,
Reihe Modeling and Simulation, Vol. 3 (Forschungszentrum Jülich, 2013), [121]
- [118] E. Pavarini, E. Koch, J. van den Brink, G. Sawatzky (Eds.):
Quantum Materials: Experiments and Theory,
Reihe Modeling and Simulation Vol. 6 (Forschungszentrum Jülich, 2016), [121]
- [119] E. Pavarini, E. Koch, R. Scalettar, and R. Martin (Eds.):
The Physics of Correlated Insulators, Metals, and Superconductors,
Reihe Modeling and Simulation, Vol. 7 (Forschungszentrum Jülich, 2017), [121]
- [120] E. Pavarini, E. Koch, A.I. Lichtenstein, and D. Vollhardt (Eds.):
DMFT — From Infinite Dimensions to Real Materials,
Reihe Modeling and Simulation, Vol. 8 (Forschungszentrum Jülich, 2018), [121]
- [121] <https://www.cond-mat.de/events/correl.html>

